Technische Universität München
Physik-Department

Master's Thesis

Study of R-parity Violating Decays of Supersymmetric Particles with the ATLAS Detector at the LHC

Stefan Raimund Maschek

München
Monday, October 17th, 2016

Max-Planck-Institut für Physik
(Werner-Heisenberg-Institut)

Technische Universität München
Physik-Department
Erstgutachter (Themensteller): Priv.-Doz. Dr. H. Kroha
Zweitgutachter: Prof. Dr. L. Oberauer

I assure the single handed composition of this master's thesis is only supported by declared resources.

Ich versichere, dass ich diese Masterarbeit selbstständig verfasst und nur die angegebenen Quellen und Hilfsmittel verwendet habe.

München, 17. Oktober 2016

Unterschrift

Abstract

Supersymmetry is a space-time symmetry that postulates the existence of new particles. It assigns to each Standard Model fermion (boson) an associated supersymmetric boson (fermion) partner with the same quantum numbers except for spin. The introduction of these new supersymmetric particles provides a potential solution to the hierarchy problem. Discovery of such particles or alternatively an exclusion of a certain supersymmetic parameter space is one of the main purposes of collider experiments.

A special scenario of Supersymmetry that enables the decay of the lightest supersymmetric particle to Standard Model particles is studied using proton-proton collision data collected by the ATLAS experiment at $\sqrt{s} = 13$ TeV. The searched signal is characterized by a final state of at least four leptons, which leads to extraordinarily low background contributions from Standard Model processes. The work described in this thesis assisted to an exclusion of the considered supersymmetric model for hypothesized mass of the lightest supersymmetric particle of up to 1.1 TeV.

Although the size of background contributions is small in this analysis, it has to be measured as precisely as possible in order to set most stringent limits on higher lightest supersymmetric particle mass regimes. This thesis concentrates on a special type of Standard Model background that does not arise in primary interaction processes but is a result of wrongly identified or secondarily emerging leptons that contribute to the four-lepton final state. A data-driven method is presented to estimate this kind of background.

Acknowledgments

Thanks to the aid of Niko Köhler and Johannes Junggeburth I was able to utilize their great new software framework within a short time. My office collegue, Dominik Krauss, always gave me quick and clear answers on every question I posed which I really appreciated.

Furthermore, I want to thank Mike Flowerdew for all the introductive lessons and for introducing me to the four-lepton analysis group. He accompanied the most of my studies with good faith and trust in my skills.

After his leaving, Tina Potter started to look after me and helped me with her advice and encouragement with the finishing of this thesis for which I am honestly grateful.

I am deeply thankful to my mother, who helped me through that difficult and exhausting time.

In the end, I want to express my gratitude to Hubert Kroha for introducing me to Atlas and giving me the opportunity of a year of very exciting studies. I really appreciate the enormous amount of work he put in to give constructive comments on my thesis even during his weekends.

Contents

Chapter 1

Introduction

The Standard Model describes particle physics in a term of Gauge Quantum Field Theories [1–3]. Matter consists of quarks and leptons which appear in three generations with increasing masses. The lightest lepton is the electron and the two lightest quarks are the components of the nucleons which build up the matter we consist of. Three of the known fundamental forces, the electromagnetic, the weak and the strong force, are described in the Standard Model by the interchange of vector bosons, like the photon in the electromagnetic interaction.

The Standard Model was developed during the second half of the 20 century. Its predictions have been successfully tested in many experiments. With the discovery of the Higgs particle in 2012 by the ATLAS [4] and CMS [5] experiments of the Large Hadron Collider (LHC) the last missing piece of the theory has been found.

However, there are also many hints that this theory is only the low-energy limit of a more complete theory. A theoretical argument is for example the enormous difference of the energy scales of the electroweak interaction in the Standard Model (10^3 GeV) and of gravity (10^{19} GeV), referred to as the hierarchy problem, which leads to a fine-tuning problem of the radiative corrections to the Higgs boson mass. The Standard Model does not describe gravity at all [6]. Experimental arguments are the astrophysical observations of dark matter [7, 8] and of dark energy [9, 10] which are not explained by the Standard Model as well as the asymmetry between matter and anti-matter, referred to as CP problem [11].

A very popular extension of the Standard Model (SM) is supersymmetry [12], which solves general problems of the SM. This symmetry relates fermions and bosons and assigns a fermionic (bosonic) superpartner to each Standard Model boson (fermion). It is strongly motivated by theoretical considerations and is one of the main purposes of particle collider experiments. In many supersymmetric models with R-parity conservation, the lightest supersymmetric particlle is neutral and stable and provides an excellent candidate for a Dark Matter particle.

A special variant of supersymmetry is R-parity violating supersymmetry [13]. It allows for the decay of the lightest supersymmetric particle into SM particles, especially into leptons, which leads to a very clean signature for supersymmetry (SUSY) at a hadron collider like the LHC, namely final states with four or more leptons.

The ATLAS [14] detector is one of the experiments at the Large Hadron Collider [15] which operated at center-of-mass energies of 7 and 8 TeV in the years 2010-2012. Searches for signatures with four or more leptons have been performed but no sign of new physics beyond the SM has been found [16]. With the start of the LHC operation of a center-of-mass energy of 13 TeV in June 2015, the searches for supersymmetry continue, including the four-lepton signature.

This thesis is concerned with the estimation of the small Standard Model background in the four-lepton SUSY search. using data-driven methods.

Chapter 2

The Standard Model and its Supersymmetric Extension

The Standard Model (SM) describes all known particles and three out of four of their interactions. It has been extensively tested in various different experiments. This chapter will introduce some basic theoretical concepts of the SM which based on the descriptions in [17]. Although the SM is very useful to describe a lot of phenomena, there are strong hints that the SM is only a part of a more complete theory. Supersymmetry (SUSY) is one possible approach to extend the SM.

In the following, natual units ($\hbar = c = 1$) are used.

2.1 Symmetries

In the framework of quantum field theory (QFT) the Standard Model describes the electromagnetic, the weak and the strong force. It describes all matter constituents by spin-1/2-fermions. The basic elementary particles are leptons and quarks, both appearing in three mass generations. They are all described by spinors, $\psi = \psi(x^\mu)$, elements of an anti-commuting Clifford algebra, which are solutions to the Dirac equation,

$$(i\gamma^\mu \partial_\mu - m)\psi = 0, \tag{2.1}$$

The Dirac equation is according to Hamilton's principle obtained from the Lagrange function,

$$\mathcal{L} = i\bar{\psi}\gamma^\mu \partial_\mu \psi - m\bar{\psi}\psi. \tag{2.2}$$

$$\psi(x^\mu) \to \psi(x^\mu - a^\mu) = e^{-ia^\mu \hat{p}_\mu}\psi(x^\mu), \tag{2.3}$$

generated by the translation operator, $\hat{p}_\mu$, which is the canonical momentum. If a translation leaves the equations of motions invariant, it means in reverse the conservation of energy and momentum, p_μ. The space-time translation forms, together with boosts and rotations in 3-dimensional space, the so-called Pointcaré algebra.

A different type of symmetries are the so called gauge symmetries,

$$\Psi \rightarrow e^{i\alpha^a \hat{\tau}_a}\Psi, \tag{2.4}$$

with a scalar phase parameter α^a, which transform the fields themselves. These fields, Ψ, may be not only the spinor fields of single particles, but multiplets consisting of different particles. As an example, electroweak doublets in the SM are,

$$\Psi = \boldsymbol{Q}_L, \boldsymbol{L}_L, u_R, d_R, e_R, \tag{2.5}$$

where u_R, d_R and e_R are singlets, whereas $\boldsymbol{Q}_L$ and $\boldsymbol{L}_L$ are doublets under the SU(2), containing and up- and down-type quark pair, or an charged lepton with its neutrino, respectively. These fields are now vector spaces to a Lie algebra spanned by N generators $\hat{\tau}_a$ ($a = 1, ..., N$) fulfilling the commutation relations,

$$[\hat{\tau}_a, \hat{\tau}_b] = if_{abc}\hat{\tau}_c, \tag{2.6}$$

with f_{abc}, the total antisymmetric structure constant of the appropriate Lie algebra.

Gauge transformations have to be local to maintain causality, i.e. in Equation (2.4) $\alpha^a = \alpha^a(x^\mu)$.

It requires the kinematic term, i.e. the derivation in Eqation (2.2) to be expressed in terms of a gauge-covariant derivative,

$$\partial_\mu \rightarrow D_\mu = \partial_\mu - igV_\mu^a(x)\hat{\tau}_a\psi(x), \tag{2.7}$$

where the so-called gauge fields V_μ^a are introduced. They require a kinematic term to be added in the Lagrangian,

$$\mathcal{L}_{\text{gauge}} = -\frac{1}{4}V_{\mu\nu}^a V_a^{\mu\nu}, \tag{2.8}$$

with

$$V_{\mu\nu}^a = \partial_\mu V_\nu^a - \partial_\nu V_\mu^a + gf^a{}_{bc}. \tag{2.9}$$

The gauge fields themselves transform under the adjoint transformation and forbids the direct insertion of common mass terms, like $m_V V_\mu V^\mu$. The gauge bosons are therefore a priory massless.

The expansion of D_μ results in terms like

$$\mathcal{L}_{\text{interaction}} = g\bar{\Psi}\gamma_\mu V_a^\mu \hat{\tau}^a \Psi, \tag{2.10}$$

describing the interaction of a gauge field, i.e. the gauge boson, to a fermion-multiplet.

2.2 Gauge Interactions and the Electroweak Symmetry Breaking in the Standard Model

The symmetry group in the SM is the direct product

$$\mathrm{U}(1)_Y \times \mathrm{SU}(2)_L \times \mathrm{SU}(3)_C. \tag{2.11}$$

The charges of the $\mathrm{SU}(3)_C$ are called colour and its gauge bosons are called gluons and are the source of the strong interaction described by Quantum Chromo Dynamics (QCD). The generators of the gauge transformation are the eight Gell-Mann matrices.

Charges of the $\mathrm{SU}(2)_L$ are described by the weak Isospin, which transform under a transformation using the three Pauli matrices. Their three gauge bosons are $W^{\pm}$ and W^3. Right handed particles transform trivially under the $\mathrm{SU}(2)_L$, whereas left handed particles form doublet according to

$$\boldsymbol{Q}_L = \begin{pmatrix} u_L \\ d_L \end{pmatrix}, \begin{pmatrix} c_L \\ s_L \end{pmatrix}, \begin{pmatrix} t_L \\ b_L \end{pmatrix} \qquad \boldsymbol{L}_L = \begin{pmatrix} \nu_{e,L} \\ e_L \end{pmatrix}, \begin{pmatrix} \nu_{\mu,L} \\ \mu_L \end{pmatrix}, \begin{pmatrix} \nu_{\tau,L} \\ \tau_L \end{pmatrix} \tag{2.12}$$

leading to a maximum parity violation by the weak interaction.

The charge associated with the $\mathrm{U}(1)_Y$ is called the hypercharge Y.

As mentioned in Section 2.1 gauge bosons are predicted to be massless. Also the mass generations of the quarks and leptons prevent the fermions to be massive under the $\mathrm{SU}(2)_L$. Particle masses are instead generated by the spontaneous symmetry breaking of the $\mathrm{U}(1)_Y \times \mathrm{SU}(2)_L$ symmetry. To realize this, a complex scalar $\mathrm{SU}(2)_L$ doublet field is introduced. This field, Φ, is exposed to an intrinsic potential $\mathcal{V}(\Phi^\dagger\Phi)$, contributing to the Lagrangian with local minimums at a so-called vacuum expectation value (VEV), $|\Phi| = v$. While the set of minima is still invariant under $\mathrm{U}(1)_Y \times \mathrm{SU}(2)_L$, the realization of one particular VEV spontaneously breaks the symmetry to an $\mathrm{U}(1)_Q$, resulting in quantum electrodynamics (QED) with its well known electric charge e. An expansion around the VEV yields

$$\Phi(x^\mu) = \begin{pmatrix} 0 \\ v + H(x^\mu) \end{pmatrix}, \tag{2.13}$$

where H is a scalar physical field, known as the Higgs field. The three lost degrees of freedom in comparison to the complex doublet field, Φ, are absorbed by three vector bosons, allowing them to carry mass.

This expansion results in Lagrangian terms that give mass to the vector bosons,

$$\mathcal{L}_{\text{Higgs}} = \frac{1}{2} g_W^2 v^2 W_\mu^+ W^{-\mu} + \frac{1}{4} v^2 \begin{pmatrix} W_\mu^3 \\ B_\mu \end{pmatrix}^T \begin{pmatrix} g_w^2 & -g_W g_Y \\ -g_W g_Y & g_Y^2 \end{pmatrix} \begin{pmatrix} W^{\mu 3} \\ B^\mu \end{pmatrix} \tag{2.14}$$

Furthermore it mixes the gauge bosons B_μ and W_μ^3 to their mass eigenstate,

$$\begin{pmatrix} Z_\mu \\ A_\mu \end{pmatrix} = \begin{pmatrix} \cos\theta_W & \sin\theta_W \\ -\sin\theta_W & \cos\theta_W \end{pmatrix} \begin{pmatrix} W_\mu^3 \\ B_\mu \end{pmatrix}, \tag{2.15}$$

Figure 2.1: Leading order Feynman diagrams of the quantum correction to the Higgs propagator, arising from couplings of fermions and bosons to the Higgs field, leading to a correction term of the Higgs boson mass.

where θ_W is the so-called Weinberg angle, related to the coupling constants g_Y and q_W of the $\mathrm{U}(1)_Y$ and $\mathrm{SU}(2)_L$ via

$$\cos\theta_W = \frac{g_W}{\sqrt{g_W^2 + g_Y^2}}. \tag{2.16}$$

Fermions obtain also their mass from the Higgs field by Yukawa couplings.

This Higgs field, H, is a massive excitation and must therefore be observable as a massive particle with spin 0. In 2012 such a scalar particle has been discovered by ATLASand CMS at the LHC.

2.3 The Hierarchy Problem and Experimental Constrains to the SM

So called loop diagrams in higher order perturbation, as shown in Figure 2.1 results in leading order correction terms to the Higgs mass of

$$m_H^2 = -\mu^2 + \Delta m_H^2 = -\mu^2 - \frac{\Lambda_{\mathrm{UV}}}{8\pi^2}\sum_f |\lambda_f|^2 \approx (125.09\ \mathrm{GeV})^2, \tag{2.17}$$

where λ_f are the Yukawa couplings of the fermions to the Higgs boson and Λ_{UV} is the energy scale up to which the SM is valid. If the SM is to be valid up to the Planck scale $m_{\mathrm{Pl}} \approx 10^{19}$ GeV, where quantum gravity is to be taken into account, the two terms of Equatin (2.17) must cancel with a precision of $m_H^2/m_P l^2 \approx 10^{-35}$, which implies a extrem fine-tuning and appears to be unnatural. This problem is referred to as the hierarchy problem.

The Standard Model does not provide solutions to the astronomical and cosmological observations of dark matter and dark energy. It neither explains the asymmetry between matter and anti-matter, known as the CP problem, and it is not compatible to any consistent quantum mechanical description of gravity. All these constrains lead to the conclusion, that the SM is not a complete theory. Supersymmetry (SUSY) is an extension of the SM and might provide solutions to some of these problems.

2.4 Supersymmetry

Supersymmetry [12] is a space-time symmetry that relates fermions with bosons. According to the Haag-Łopuszański-Sohnius-Theorem theorem there is only one non-trivial extension of the Pointcaré algebra, as the generators of space time translation, is the anti-commuting spinoral operator, $\hat{Q}$, which transforms fermionic fields to boson fields and vice versa:

$$\hat{Q}|f\rangle = |B\rangle \tag{2.18}$$

$$\hat{Q}|B\rangle = |f\rangle \tag{2.19}$$

This operator commutes with the generators of the space-time translation, the momentum, as well as with the generators of the gauge groups explained in Section 2.2, thus fermions and bosons related by the SUSY operator can be expressed with the same eigenstates and transform equally under the gauge transformations. This results in the same couplings and masses for the boson fermion pair.

These pairs are called superpartners and their spin differs by 1/2. One can represent them as so-called supermultiplet. They consist either in a chiral spinor field and one scalar field, forming a chiral supermultiplet, or in a gauge boson with a so-called gaugino. Latter must transform, as its superpartner, equally for right- and left handed components and is thus not chiral. Gauge boson and gaugino form a so-called a gauge supermultiplet.

The missing evidence of SUSY particles with equal mass as their superpartners leads to the assumption, that SUSY is a broken symmetry. There are may ways to break SUSY by introducing extra mass terms for the superpartners [18], which would explain the mass discrepancy. These additional mass terms lead to a non-vanishing correction term to the Higgs boson mass which can be expressed as

$$\Delta m_H^2 = m_{\text{soft}}^2 \left(\frac{\lambda}{16\pi^2} \ln \frac{\Lambda_{\text{UV}}}{m_{\text{soft}}} + ... \right), \tag{2.20}$$

where m_{soft} is the scale of these additional masses particles and λ is a dimensionless coupling. To maintain the capability of SUSY to solve the hierarchy problem, m_{soft} must not exceed few TeV. This offers the possibility of the production of at least the lightest supersymmetric particles at the LHC.

The minimal particle content in a supersymmetric theory is implemented in the so-called Minimal Supersymmetric Standard Model (MSSM). The bosonic superpartner of quarks and leptons are called squarks and sleptons respectively. The associated chiral superfields for quarks are,

$$\boldsymbol{Q}_i = \begin{pmatrix} Q_{L,i} \\ \tilde{Q}_{L,i} \end{pmatrix}, \qquad \bar{\boldsymbol{U}}_i = \begin{pmatrix} u_{R,i}^\dagger \\ \tilde{u}_{R,i}^* \end{pmatrix}, \qquad \bar{\boldsymbol{D}}_i = \begin{pmatrix} d_{R,i}^\dagger \\ \tilde{d}_{R,i}^* \end{pmatrix}, \tag{2.21}$$

where i indicates the quark family. $\boldsymbol{Q}_i$ contains the left handed quarks, and its superpartner, transforming as doublet under the electroweak gauge group, whereas $\bar{\boldsymbol{U}}_i$ and $\bar{\boldsymbol{D}}_i$ consists of the right handed anti-quarks and its superpartner, which transform as singlets under the $SU(2)_2$. Analogously, the superfields of the leptons are,

$$\boldsymbol{L}_i = \begin{pmatrix} L_{L,i} \\ \tilde{L}_{L,i} \end{pmatrix}, \qquad \bar{\boldsymbol{E}}_i = \begin{pmatrix} e_{R,i}^\dagger \\ \tilde{e}_{R,i}^* \end{pmatrix}, \tag{2.22}$$

Table 2.1: Particle content of the Minimal Supersymmetric Standard Model (MSSM).

Standard Model Particles			**Superpartners**		
Quarks	$u \quad c \quad t$ $d \quad s \quad b$		$\tilde{u} \quad \tilde{c} \quad \tilde{t}$ $\tilde{d} \quad \tilde{s} \quad \tilde{b}$		**Squarks**
Leptons	$\nu_e \quad \nu_\mu \quad \nu_\tau$ $e \quad \mu \quad \tau$		$\tilde{\nu}_e \quad \tilde{\nu}_\mu \quad \tilde{\nu}_\mu$ $\tilde{e} \quad \tilde{\mu} \quad \tilde{\tau}$		**Sleptons**
	Electroweak symmetry broken	 unbroken	Unknown mixing		
EW gauge bosons	A_μ Z_μ $W_\mu^\pm$	B_μ W_μ^3 $W_\mu^\pm$	$\tilde{B}$ $\tilde{W}$ $\tilde{W}^\pm$	$\tilde{\chi}_i^0$	**Neutralinos** $(i = 1, ..., 4)$
SM like Higgs boson	h	$\begin{pmatrix} H_u^+ \\ H_u^0 \end{pmatrix}$	$\begin{pmatrix} \tilde{H}_u^+ \\ \tilde{H}_u^0 \end{pmatrix}$	$\tilde{\chi}_j^\pm$	**Charginos** $(i = 1, 2)$
Additional Higgs bosons	H A $H^\pm$	$\begin{pmatrix} H_d^0 \\ H_d^- \end{pmatrix}$	$\begin{pmatrix} \tilde{H}_d^0 \\ \tilde{H}_d^- \end{pmatrix}$		
Gluons	$g_\mu^i \ (i = 1, ..., 8)$		$\tilde{g}_\mu^i \ (i = 1, ..., 8)$		**Gluinos**

where again i denotes the lepton generation.

Ferminonic superpartners of bosonic fields have the suffix -ino appended. Because the SUSY operator commutes with the unbroken electro-weak gauge group, fermionic partners are assigned to the unbroken vector fields B_μ, and W_μ^i. Their superpartners are called "bino" and "wino", or summarized "gauginos". It is shown [12] that the minimum number of degrees of freedom of the unbroken the Higgs field in a supersymmetric model must be eight, resulting in 5 physical Higgs bosons h, H, A and $H^\pm$. Therefore, there are also 8 higgsino of which 2 carry electromagnetic charge. Because higgsinos and gauginos share the same quantum numbers regarding the gauge groups, they can potentially mix similar to the electroweak mixing in the SM. Resulting charged fermions are named charginos, $\tilde{\chi}_i^\pm$ $(i = 1, 2)$, numbered by their mass hierarchy, whereas the resulting neutral fermions are called neutralinos, $\tilde{\chi}_i^0$ $(i = 1, 2, 3, 4)$. If a chargino or neutralino is called bino-like or wino-like, it is assumed to have a major mixing component of bino or wino, respectively.

Related to the Standard Models Lagrangian, a concept called the superpotential [12] relates coupling constant parameter to allowed interactions. The superpotential of the MSSM is the continuation of the Higgs potential in the Standard Model Lagrangian to the formalism of Superfields,

$$W_{\text{MSSM}} = y_u^{ij}\bar{\boldsymbol{U}}_i\boldsymbol{Q}_j H_u - y_d^{ij}\bar{\boldsymbol{D}}_i\boldsymbol{Q}_j H_d - y_e^{ij}\bar{\boldsymbol{E}}_i\boldsymbol{L}_j H_d + \mu H_u H_d, \tag{2.23}$$

where y_{ij} are the dimensionless Yukawa couplings which describe interactions beween the Higgs and the matter superfields and μ is the Higgs mass parameter.

R-Parity [13, 19] is a multiplicative quantum number arising from a discrete symmetry and is related to the lepton, L, and baryon number, B, conservation. It is conserved in the MSSM superpotential. The R-parity can be expressed as

$$P_R = (-1)^{3(B-L)+2S} = \begin{cases} 1 & \text{for SM particles} \\ -1 & \text{for SUSY particles} \end{cases}, \tag{2.24}$$

where S indicates the spin of the particle. If R-parity is violated (RPV), additional baryon and lepton number violating terms may be added to equation (2.23):

$$W_{\text{RPV}} = \frac{1}{2}\lambda_{ijk}\boldsymbol{L}_i\boldsymbol{L}_j\bar{\boldsymbol{E}}_k + \lambda'_{ijk}\boldsymbol{L}_i\boldsymbol{Q}_j\bar{\boldsymbol{D}}_k + \kappa_i\boldsymbol{L}_i H_u + \frac{1}{2}\lambda''_{ijk}\bar{\boldsymbol{U}}_i\bar{\boldsymbol{D}}_j\bar{\boldsymbol{D}}_k, \tag{2.25}$$

where λ_{ijk}, λ'_{ijk} and λ''_{ijk} are dimensionless Yukawa coupling constants and κ_i has the dimension of mass and vanishes at the unification scale. λ_{ijk} as well as λ''_{ijk} are anti-symmetric in the indices i and j, satisfying $\lambda_{ijk} = -\lambda_{jik}$. The first three terms in Equation (2.25) violate lepton number, wheras the last term violates baryon number.

2.5 Concidered SUSY Signature

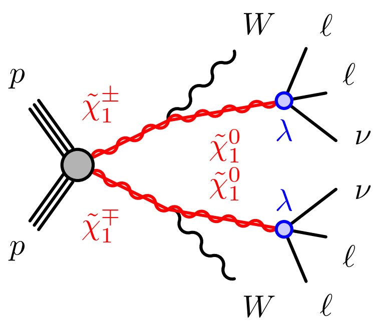

Figure 2.2: Diagram of the benchmark SUSY model of chargino production with indirect RPV decays.

The simultaneous existence of non-vanishing λ_{ijk} and λ''_{ijk} terms would allow for proton decay [12] that is in conflict to observations. This can be avoided, by explicitly by explicitly conserving either B or L in the Lagrangian in RPV scenarios. In RPV models, the lightest SUSY particle is unstable and decays to SM particles, including leptons when at least one of the λ_{ijk} parameters is non-vanishing. RPV scenarios can thus result in final states with high lepton multiplicities and a measured unbalanced momentum conservation in the detector. These allow for a selection to suppress SM background effectively.

A search for new physics with at least four isolated electrons or muons in the final state was reported at ICHEP [20]. This analysis, to which the work in this thesis has contributed, follows closely the 7 TeV and 8 TeV analyses [16]. The search itself is model-independent but is optimized for a signature resulting from a certain simplified benchmark model. The results are furthermore interpreted in terms of this bechmark model.

The benchmark model consists in wino-like charginos and a bino-like neutralino as lightest supersymmetric particle (LSP). Figure 2.2 shows the pair-produced $\tilde{\chi}_1^{\pm}$ decaying to the LSP while emitting a W boson. The subsequent $\tilde{\chi}_1^0$ decay is mediated by the $\frac{1}{2}\lambda_{ijk}\boldsymbol{L}_i\boldsymbol{L}_j\bar{\boldsymbol{E}}_k$ term in Eq. 2.25, allowing each LSP to undergo a lepton-number-violating RPV decay:

$$\tilde{\chi}_1^0 \rightarrow \ell_k^{\pm}\ell_{i/j}^{\mp}\nu_{j/i}, \tag{2.26}$$

with the lepton flavors depending on the indices of the associated λ_{ijk} couplings. Therefore, every signal event contains at least four charged leptons, and potentially up to two further for each Wboson decaying leptonically.

In principle, the nine λ_{ijk} RPV couplings allow the $\tilde{\chi}_1^0$to decay to every possible combination of charged lepton pairs. The scenarios considered in this analysis include only decays to electrons and muons. The decays $\tilde{\chi}_1^0 \rightarrow e^+e^-\nu$, $\tilde{\chi}_1^0 \rightarrow e^{\pm}\mu^{\mp}\nu$ and $\tilde{\chi}_1^0 \rightarrow \mu^+\mu^-\nu$ have each a branching fraction of 1/3. Terms with non-zero values of the λ_{121} and λ_{122} couplings can give rise to these $\tilde{\chi}_1^0$ decays. In this thesis these SUSY scenarios are referred to as $LL\bar{E}12k$ ($k = 1, 2$). However, the $\tilde{\chi}_1^0$ branching fractions cannot be reproduced by a single non-zero $LL\bar{E}$ coupling. "Pure" coupling scenarios are obtained by appropriate reweighting of the simulated events, analogous to the procedures used in Ref. [21].

Within the $LL\bar{E}12k$ scenarios, chargino masses of $500 - 1200$ GeV are studied and LSP masses range from 10 GeV $\leqslant m(\tilde{\chi}_1^0) \leqslant m(\tilde{\chi}_1^{\pm}) - 10$ GeV. It is chosen thus to ensure the RPC cascading of $\tilde{\chi}_1^{\pm}$ as well as the $\tilde{\chi}_1^0$ LSP decay to be prompt. Over this chargino mass range, the $\tilde{\chi}_1^+\tilde{\chi}_1^-$ production cross-section varies from about 22 fb to about 0.2 fb [22, 23].

Chapter 3

The ATLAS detector at the LHC

3.1 The Large Hadron Collider

The Large Hadron Collider [15,24] is the worlds largest circular particle accelerator opperated by the European Organization for Nuclear Research (CERN) located near Geneve in Swiss. It has a circumferrence of of 26.7 km. It was built within the tunnels of the precessor accelerator, the Large Electron Positron Collider (LEP) and lies in an depth of 150 m under ground in the border region between Swiss and France.

A chain of preaccelerating devices injects proton beams into the LHC. Starting with a linear accelerator , the LINAC 2 it passes two synchrotrons , the Proton Synchrotron (PS) and the Super Proton Synchrotron (SPS), the beam reaches 450 GeV, before entering in the two opposite directions the LHC. Here can be accelerated to the design energy of up to 7 TeV.

The LHC provides beams, among others, to the four main experiments, ALICE, LHCb, CMS and ATLAS. The ALICE detector investigates the quark gluon plasma and the LHCb does researches for b-quark physics. The both multipurpose devices CMS and ATLAS are designed for precision measurements in the Standard Model and are testing for possible phenomena beyond the Standard Model.

Design Capacity And Current Performance of the LHC

During optimal conditions the proton beam consists of trains with up to 72 bunches. Each bunch contains about 1.210^{11} protons seperated by a bunch spacing of 25 ns. At design luminosity which is nominal $10^{34}\text{cm}^{-2}\text{s}^{-1}$ there are up to 2808 bunches per beam.

The event rate is determined by the instantaneous luminosity which is defined as

$$\mathcal{L} = \frac{Nn\nu}{4\pi d_x d_y}$$

where N denotes the number of bunches and n the number of protons per bunch, ν is the revolution frequency of the beam and $d_{x,y}$ is the transverse beam size at interaction point. The event rate of a single physics process depents on the luminosity over its total cross section σ according to the relation

$$R = \sigma\mathcal{L}$$

A high luminosity do not only increase the rate of the wanted events, but also the rate of further events within one bunch crossing, which contaminates the the resolution of the event of interest. This effect is referred to as pile-up. It is quantified by the μ-value, the number of events per bunch crossing.

The increase in steepness between the 2015 and 2016 illustrates the effect of a ramp up in luminosity during the Christmas shutdown which results in different μ profiles.

The total yet accumulated luminosity in September 2016 is about 30 fb^{-1}.

3.2 The ATLAS detector

ATLAS (A Toroidal LHC ApparatuS) [14] is a multi-purpose particle detector to measure proton-proton collisions at the LHC. It has a forward-backward symmetric cylindrical geometry mounted around the beam. It can be divided in two basic regions, the barrel region and the end caps, covering almost the entire solid angle around the interaction point. The barrel is mounted concentric around the beam line, whereas the disk shaped end caps are arranged perpendicular to the beam.

3.2.1 Coordinate System

ATLASuses a right handed coordinate system with the origin in the interaction point. Is x-axis points inwards the LHC ring, the y axis upwards and the z-axis along the beam line. In the analysis a polar coordinate system is used with the variables r, ϕ and η, defined as

$$r = \sqrt{x^2 + y^2}, \tag{3.1}$$

$$\phi = \arctan\frac{y}{x}, \tag{3.2}$$

$$\theta = \arctan\left(\frac{z}{\sqrt{x^2 + y^2}}\right), \tag{3.3}$$

where θ is the common polar coordinate measured with respect to the z-axis. The 4-momentum of out flying inelastic scattered paricles is described by the variables p_{T}, η, ϕ and the mass m, where

$$\eta = -\ln\left(\tan\frac{\theta}{2}\right), \tag{3.4}$$

$$p_{\mathrm{T}} = \sqrt{p_x^2 + p_y^2} = |\boldsymbol{p}| \cdot \frac{1}{\cosh\eta,}, \tag{3.5}$$

where η is the so-called pseudo-rapidity and is used to describe the polar angle. Is corresponds in the massless limit to the rapidity of the Lorentz boost along the beam axis which takes an observer from the lab frame to a frame in which the particle moves only perpendicular to the beam. p_{T} is the transverse momentum. The angular distance between two vectors from their interaction point is measured by

$$\Delta R = \sqrt{(\Delta\eta)^2 + (\Delta\phi)^2}. \tag{3.6}$$

Charged particle tracks are described by five parameters, d_0, z_0, θ, ϕ and q/p. q is the particles charge and (p, θ, ϕ) is the momentum vector at the closest approach to the beam line. d_0 and z_0 are the so-called transverse and longitudinal impact parameter. They discribe the point of closest approach of the extrapolated trajectory to the primary interaction point.

The detector is build up of three subsystems, the inner detector which precisely measures the trajectories of of charged particles, the calorimeter system which measures energy deposits of electromagnetically or strongly interacting particles, and the muon spectrometer, that measures the only charged Standard Model particle, that is able to escape the calorimeters.

3.2.2 The Inner Detector

The innermost subsystem of of ATLASis the inner detector. It measures the trajectories of charged particles, referred to as tracks. The tracks are bended by a homogeneous magnetic field of $2T$ oriented parallel to the beam line allowing to measure particles charge and momentum. The tracks are also used to reconstruct primary and potential secondary interaction points (vertices). The ID covers a pseudo-rapidity region of $|\eta| < 2.5$ This is achieved by an interplay of three different parts, the pixel detector, the semiconductor tracker and the transition radiation tracker.

The pixel detector is the part closest to the beam line, it consists by now of four concentric layers of silicon pixel sensors with a high granularity mounted between 33 and $122.5mm$ from the beam line in the barrel and tree disks in the end caps at distances between 50 and $65cm$. Its granularity provides a resolution of $10 \times 115\mu m$ (arranged along the bending plane) is crucial to reconstruct the interaction vertices precisely.

The second part of the inner detector is the so-called semiconductor tracker. It is made up of silicon micro strip detectors, arranged parallel to the y-axis, which provides a resolution of $17 \times 580\mu$m and are thus somewhat coarser than the pixel detector. It consist of four concentric layers with distances between 30 and 51 cm in the barrel and nine disks in the end caps at distances between 85 and $272cm$ from the nominal interaction point.

The third inner detector part is placed outside the SCT in a distance of 55 - 100 cm. Transition radiation trackers are straw drift tubes with a diameter of 4 mm filled with a Xe-CO_2-O_2 gas mixture also oriented along the z-axis. They can measure charged particles with a resolution of 130 μm in R-ϕ direction, while no η-information is provided. Electrons passing through the polypropylene radiator material interleaved between the tubes emit radiation that is detected by the straw tubes and allows the TRT to contribute to the identification of electrons.

3.2.3 The Calorimeter System

The calorimeter system measures particle energies by absorbing them. For the reconstruction of the momentum balance in transverse direction, it is important to cover the solid angle as far as possible. Therefore the calorimeter system covers a pseudo-rapidity range of $|\eta| < 4.9$. Furthermore, high energy resolution for particles and jets are required. The calorimeters are finely segmented in three dimensions for angular measurements of showers, for matching them to inner detector tracks and for the identification of electrons, photons and hadron jets. The calorimeters are kept thick enough in order to prevent particle showers to fully penetrate the calorimeters and be misidentified as muons in the outermost subsystem. The calorimeter system is divided into three subsystems, the electromagnetic calorimeter (ECAL), the hadronic calorimeter (HCAL) and the forward calorimeter (FCAL).

The electromagnetic calorimeter uses electromagnetic particle showers to measure energies of electrons and photons. It covers the pseudo-rapidity region of $|\eta| < 3.2$. Accordion shaped lead plates are used as absorber material, whereas liquid argon (LAr) as active material in the thin gaps between the plates ionizes and is collected by electrodes. To reduce noise, the calorimeter is housed in a cryostat.

The hadronic calorimeter surrounds the ECAL and has the purpose of measuring strongly interacting particles that escape it. The HCAL consists of a barrel tile calorimeter in the region $|\eta| < 1.7$ and two LAr sampling endcap calorimeters for $1.5 < |\eta| < 3.2$. The tile barrel calorimeter uses scintillating tiles as active material and steal as absorber plates, whereas in the end caps LAr is used as active material and copper plates as absorber material.

To forward calorimeter covers regions of high pseudo-rapidity between 3.1 and 4.9 and consists of one module optimized for electromagnetic and two for hadronic calometry. Both using LAr as active material, the electromagnetic module uses copper as absorber and the hadronic modules use tungsten to antagonize the high background due to the closeness to the beam line.

3.2.4 The Muon Spectrometer

The muon spectrometer is the outermost subsytem of the ATLAS detector. It is able to identify muons with an extraordinary certainty and measure their momenta with a precision of about 3% for muons with energy around 100 GeV and a 10 % precision for muons with 1 TeV. In total it covers a pseudo-rapidity range of

$0.1 < |\eta| < 2.7$. Its principle is similar to that of to the inner detector, it measures the bending of the trajectory in a magnetic field, which is induced by eight air-core superconducting coils. to measure the trajectories it uses two different types of chambers, a precicion tracking chamber with a high spatial resolution and trigger chambers with a high temporal resolution.

The precicion chambers are necessary for accurate measurement of the momentum. Two different types of precision chambers are used in the MS. The chambers used in most of the MS are the Monitored Drift Tubes (MDT), consisting of six to eight layers of 30 mm thick aluminium drift tubes. The tubes are filled with Ar-CO_2 gas mixture and have a wire placed in the center. Bypassing muons ionize the gas and by means of the ions drift time to the wire a spacial resolution of $80\mu m$ is possible in the plane perpendicular to the tubes. The chambers are mounted tangential to the magnetic field to optimal resolve the trajectory in the bending plane. In total there are 3 layers of precision chambers. Near the beam pipe, the high background rates require the use of a different chamber technology. The Cathode Strip Chambers (CSC) are multiwire proportional chambers with a cathode strip read-out.

The disadvantage are high maximal drift time of about $700ns$. This makes it impossible to assign the muon to an specific event which happen with bunch crossing time of $25ns$. Also the arrangement of the precision chambers do not provide ϕ-information. Trigger chambers are made up by Resistive Plate Chambers (RPC) and Thin Gap Chambers (TGC). They have time resolution of about 4 ns and provide a L1 trigger information and the possibility to measure the ϕ coordinate. The RPC are installed in the barrel, whereas the TGC are used in regions close to the beam.

.

3.2.5 The Trigger System

The high luminosity of the LHC provides a large event rate. The bunch-crossing rate is 40 MHz and each bunch-crossing produces around 40 events. Assuming the information contained in each event is about one Megabyte the recording of every event would require capacities in storage and bandwidth of tens of Terabytes per second. But since only a small fraction of those events is of interest the events may and must filtered by a so-called trigger system.

A three-level trigger system [25,26] selects events to be recorded for offline analysis.

The first trigger stage, Level 1 (L1), is a hardware trigger with a latency of only 2.5 μs. It uses an approximate momentum measure from the muon trigger chambers and energy clusters from a coarser calorimeter segmentation as input to filter for potentially interesting events with highly energetic muons or calorimeter clusters. It reduces the event to aboout 100 kHz.

The second trigger stage, Level 2 (L2), runs simplified reconstruction algorithms on certain η-ϕ regions selected by the L1 trigger. It is ran on a computer farm outside the detector and due to it is only using a small fraction of the total event information, the L2 is able to make its decision within 40 ms. The L2 trigger reduces the event rate further to a few kHz.

Eventually, the Event Filter (EF) performs a reconstruction close to the final offline reconstruction algorithms. It needs several seconds for its decision to reduce the event rate further to few hundred Hz which are possible to be written on disk for later analysis.

L2 and EF are together referred to as High Level Trigger (HLT). HLT includes highly energetic charged leptons, jets, photons and even missing transverse momentum.

Thanks to the ramp ups of the LHC luminosity the data rate still increases. This makes it necessary to tighten the criteria on the triggers to stay within the available bandwith. This may be achieved by demanding higher energy thresholds or higher object multiplicities, as for example a dilepton or even trilepton trigger. But to still be capable of investigating in events that were only triggered by low engergy and multiplicity triggers another way of reduciing the event rate is the so-called trigger prescaling. It means, the trigger menu records only every F_{PS}th event selected by the prescaled trigger, while F_{PS} is the so-called prescale factor.

Chapter 4

Simulation and Event Reconstruction

4.1 Monte Carlo Event Generation and Detector Simulation

To test physics models, Standard Model physics as well as new physics beyond the Standard Model, Monte Carlo (MC) generators are used to simulate their signatures within the detector and to compare data and theoretical predictions. The production of MC samples is subdivided in three different steps: The event generation, the detector simulation and the reconstruction.

The event generation itself consists in different sub steps. The process's differential cross section is determined perturbatively at either leading order (LO), next-to-leading order (NLO) or even to further perturbation order (NNLO,NNNLO,...). Since the interacting particles are partons with unknown momenta within the protons, the cross-section has to be convoluted with the so-called Parton Distribution Functions (PDF). This process is referred to as hard process. The remaining partons perform themselves scattering processes, referred to as underlying event, that are not included in the primary process cross-section and are described by the UE tune. Subsequently, quarks and gluons created in the hard process hadronize which is described by the so called showering algorithms. The hadronization is performed in energy regions where the strong coupling $g_s \gtrsim 1$ is not possible to be described perturbatively anymore and is thus now calculated in the cross-section.

There is a huge variety of MC generators used in ATLAS, each with weaknesses and strengths with respect to the different subtasks mentioned above. Therefore, for the production of samples in ATLASmixtures of different generators are used to exploid the advantages of each single generator, depending on the relative importance.

The strengths of the generators used in this thesis are as follows. Phythia 6/8 [27–29] and Sherpa [30, 31] are multipurpose generators at LO and takes into account all the subtasks. Madgraph [32] is used to simulate additional jets, but is unable to simulate underlying events or hadronization. PowHeg [33] and MC NLO [34] provide NLO of the hard process. Often one drops the simulation of the showering performed by the generators above and reprocesses it with EvtGen to ensures consistency across generators for hadronization. However Phythia8B, which is specialized for the showering of b-hadrons, is not compatible to EvtGen.

Usually, particle filters are applied, to select only processes with the desired particles and to reduce the number of events to save computing resources by rejecting uninteresting events before process the full simulation.

Additional simulated pile-up and soft proton interactions are added to incorporate the effect of multiple proton-proton collisions in the same or nearby bunch crossings (in-time and out-of-time pile-up).

The next step is the simulation of the detector [35]. The Geant4 [36] software frameworks simulates the propagation of the final state particles throug the detector. It simulates interaction with the detector material and the magnetic field as well as electronic responses of the sensitive parts of the detector to the particles.

In the third step, the simulated events are then reconstructed using the same algorithms as data events. Information from the event generation step is referred to as truth-level information. Truth particles may be assigned to reconstructed particles and classified by their origin, referred to as truth classification.

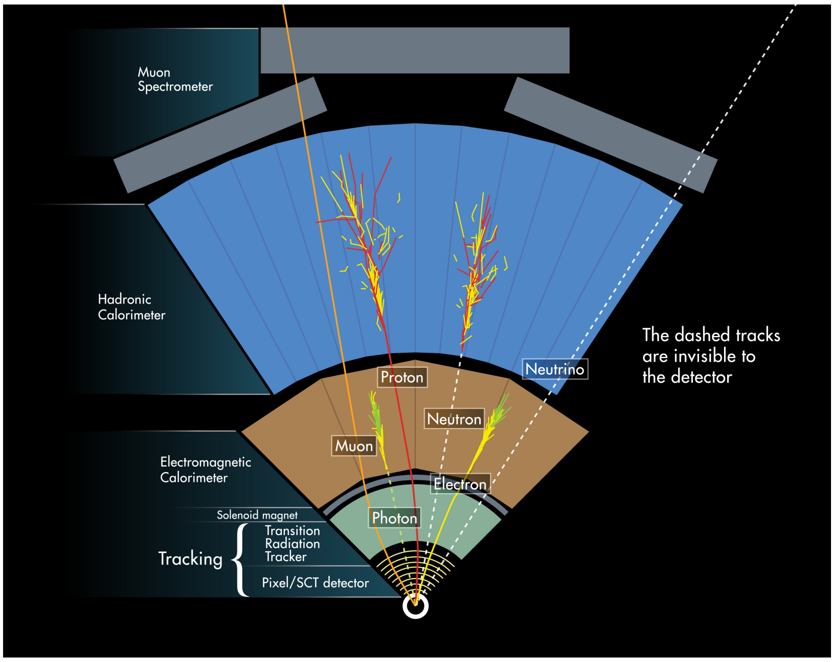

Figure 4.1: Different particle signatures in the ATLAS detector [37].

4.2 Event Reconstruction

For a further physics analysis, hits measured by the detector have to be processed to more manageable data sets that define particles and distinguish their signatures. Some particles, such as the muons, have a quite unique signature whereas others, like the different hadrons are difficult to separate and are therefore summarized with the term "jets". Neutrinos are even totally invisible to the detector and are only traceable by a momentum imbalance. They all are concluded to "objects" and have to be reconstructed by the ATLAS software. The following sections describe the basic signatures of objects and how they are reconstructed.

The base for the reconstruction of the majority of particles and the vertices are the so-called tracks. They are the trajectories of bypassing charged particles hitting single parts in the inner detector. Seeded by the innermost hit in the pixel detector, the track is extrapolated outwards and fitted to further hits in the pixel detector, the SCT and the TRT. Fake tracks are rejected based on the number of missing hits within the inner detector.

Inner detector tracks do only have momentum vectors with a pseudo-rapidity $|\eta| < 2.5$ due to the limited coverage of the inner detector.

A separate tracking is done in the muon spectrometer based on the hits in the muon chambers. They are later combined to the ID tracks.

Because the number of interactions per bunch crossing is of the order of 40, it is essential to assign the particles to a common origin and hence to a certain event. Tracks within a region of similar impact parameters are collected to form a smaller set of associated track candidates. This is done to speed up the processing and to reduce misidentifications. The primary and potential secondary vertices are reconstructed by extrapolating the selected ID tracks and using a best fit of these to determine their common origin. The primary vertex is that one, whose sum of all associated track's squared p_T is highest. The impact parameters, d_0 and z_0 are calculated with respect to this primary vertex. An event is used for the analysis if the reconstructed primary vertex has at least two tracks with transverse momentum $p_T > 400$ MeV associated with it.

Electron identification

Electron identification [38, 39] is based on a energy deposit in the electromagnetic calorimeter ECAL without significant deposit in the hadronic calorimeter.

Starting with an energy deposit of at least 2.5 MeV in the ECAL, tracks are extrapolated and associated to that cluster based on separation in ϕ-η space. Additional criteria are used to select the primary track from all associated tracks. If there is at least one track associated to the cluster, it is identified as electron, otherwise as photon.

The electrons energy is determined in the calibrated cluster, while it's direction of flight and its charge is reconstructed from the primary track.

Further identification algorithms use the ECAL shower shapes in each layer of the calorimeter and the quality of the primary track to further discriminate potential misidentified hadrons and converted photons on a likelihood base.

Four working points are defined: "tight", "medium" and "loose". The fourth commonly not used working point, "very loose", has an even better efficiency than loose is mentioned here, as it is used in this analysis. By loosening the strictness of the quality criteria one trades purity against efficiency. The efficiencies range from 80% for the very pure, tight selection to almost 100% for the very loose selection with a high rate of misidentification.

Muon Identification

The muon identification [40, 41] uses a combination of tracks in the inner detector and the muon spectrometer, MS, as well as an energy deposit in the calorimeters that is compatible with a minimum ionizing particle. It might also be reconstructed, if parts of or even a whole track is missing and thus it has the highest reconstruction efficiency in ATLAS.

Muons are classified by their four different types of reconstruction methods.

Combined muons are the most reconstructed muons in ATLAS. They are identified by a pair of matching ID and MS tracks. If the tracks in such a pair are compatible to each other, a common track is refitted to them allowing a high precision of the muons momentum.

Standalone muons do only have a MS track, which is most usefull to reconstruct muons in a pseudo-rapidity region of $2.5 < |\eta| < 2.7$ which is covered only by the muon tracking chambers but not by the ID.

Segment-tagged muons may recover low momentum muons that were not able to penetrate the whole muon spectrometer and have therefore no complete track in the MS. Inner detector tracks are extrapolated and matched to each individual hit in the muon chambers. They are identified as muons if there is a track segment along the extrapolated track.

Calorimeter-tagged muons are used to reconstruct muons with $|\eta| < 0.1$. The MS is only partially instrumented here, because clamping and wiring systems are located here. An inner detector track is identified as muon if the extrapolated track matches with a energy deposit in the calorimeters compatible with a minimum ionizing particle.

The purity of the latter two is worse due to the rejection of decaying light mesons being more difficult without an independent MS track.

Similar to electrons there are additional muon quality criteria discriminating fake muons due to misidentification from light meson decays in different levels of strictness.

While the "loose" selection maximizes the efficiency, the "tight" and "high-p_{T}" selection are optimized for purity for low and high transverse momenta respectively.

The selection used in this analysis is throughout "medium". It requires the muon to have a full MS track, thus to be either standalone or combined. It rejects candidates based on the number of missing hits. It has an efficiency of about 99%.

Jet reconstruction

Reconstructed jets consists of energy deposits in calorimeters, ECAL and HCAL, with associated tracks in the inner detector. The reconstruction is seeded by three dimensional topological connected calorimeter cells, starting with a cell of a signal-to-background ratio greater than four and iteratively adding neighbouring cells with comparative ratio. The reconstruction algorithm used in this analysis is the anti-k_T-algorithm [42] with a radius parameter of $R = 0.4$ and the three dimensional cluster mentioned above.

Energy is not only deposited in the sensitive material inside the detector, which requires to calibrate the measured deposit by the so-called jet energy scale parameter, which is derived from simulation.

Pile-Up Jets

With an average number of interactions of the order of 40, calorimeter clusters are not necessarily induced by hadrons arising in the primary vetex. Jets arising from other interaction points are referred to as pile-up jets. One can discriminate them if by requiring a significant fraction of the tracks associated with each jet originating from the primary vertex. This is done by the jet vertex tagger (JVT) [43].

b-Tagging

Jets that arise from the hadronization of b-quarks are distinguishable from other jets on a likelihood base. The relatively long living b-quark decays after about 1.5 ps [44] in a secondary vertex.

The MV2c20 algorithm [45] searches for such secondary vertices within the cone of the jet and might tag a jet with an efficiency of 77% while the misidentification rate of light flavor jets is just about 1%.

To reduce the effect of large calorimeter noise and noncollision backgrounds, events are rejected if they contain jets failing dedicated quality requirements.

Missing Transverse Momentum

Neutrinos do not interact electromagnetically and are thus invisible for ATLAS. Nevertheless, the imbalance in momentum conservation infers the presence of undetected, escaping particles.

Because spectator partons within the collision may escape along the beam line, the longitudinal component of the momentum is not known and difficult to reconstruct. Anyway, because the transverse momentum of the colliding partons is negligible, the decay product's momenta in the transverse plane must add up to zero.

The so-called missing transverse momentum [46] is defined for each component, x and y, as

$$E_{x/y}^{\text{miss}} = - \sum_{i \in \text{objects}} E_{x/y}^{i} - \sum_{j \in \text{soft terms}} E_{x/y}^{j}, \tag{4.1}$$

where the first term sums over the momenta of a certain selection of objects, defined in Section 5.1. These momenta are commonly determined over the calibrated energy deposit in the calorimeters, this is why the letter E is used. The second so-called soft term is calculated from ID tracks associated with the primary vertex with $p_{\text{T}} > 400$ MeV and further quality requirements but not associated with any of the selected objects.

A frequently used variable is the magnitude of the transverse momentum, the missing transverse energy,

$$E_{\mathrm{T}}^{\mathrm{miss}} = \sqrt{(E_x^{\mathrm{miss}})^2 + (E_y^{\mathrm{miss}})^2}. \tag{4.2}$$

4.3 Lepton isolation

Standard Lepton Isolation

This section follows the descriptions in [47] To distinguish between leptons coming from the primary process from those arising from (semi-)leptonic decays of hadronic activities a criterion named isolation is introduced. It uses detector activities in the vicinity of the lepton to decide if a lepton is regarded as isolated or not. To quantify this activities there are two basic kind of parameter defined, based on the measurements in two distinct parts of the detector, the inner detector and the calorimeter system.

The first is the $p_{\mathrm{T}}^{\mathrm{cone}}$. It is the sum of inner detector tracks in a cone with a certain radius around the lepton that are not associated to itself. The second parameter is the $E_{\mathrm{T}}^{\mathrm{cone'}}$, which sums the transverse energy deposit in a cone around the lepton with the core region excluded.

The higher the $p_{\mathrm{T}}^{\mathrm{cone}}$ in comparison to the p_{T} of the lepton, the higher is the propability of a non-isolated lepton.

The isolation tool decide on the base of these parameters. if a lepton is regarded as isolated or not There are two types of working points for the isolation tool. One uses a fixed cut on one or both of the parameters. The other approach is to define a target efficiency for isolated leptons. The cut parameters are then chosen such to fit this efficiency, based on a MC simulation of a $Z \to \ell\ell$ process. In this analysis a efficiency of 95% (99%) for leptons with transverse momentum of 25 GeV (60 GeV) is demanded.

Isolation Correction

The isolation procedure also considers two close-by leptons to be non-isolated. Such topologies are quite usual for the signal processes regarded in this analysis, especially for low LSP masses. They are originated in a prompt process and therefore wanted to be considered as isolated.

To avoid that the two leptons cause each other to be regarded as non-isolated, a correction is applied [47]. this correction substracts the contributions of the second lepton from the both variables $p_{\mathrm{T}}^{\mathrm{cone}}$ and $E_{\mathrm{T}}^{\mathrm{cone'}}$ and reapplies the cuts as normal.

Chapter 5

Four-Lepton Event Selection

This chapter is to a large part taken from the support note to the ATLAS four-lepton search paper [20] to which I have contributed.

5.1 Object Definition

As a first step towards the event selection, the objects used in the analysis, electrons, muons and jets, are defined, based on the ATLAS reconstruction and identification algorithms (c.f. Section 4.2). The ATLAS SUSY working group recommendations are adjusted to the specific needs of the analysis to achieve highest possible sensitivity for the $\tilde{\chi}_1^+\tilde{\chi}_1^-$-benchmark model, in particular for collimated signatures induced by highly boosted $\tilde{\chi}_1^0$.

To enable a data-driven estimation of the reducible background, the object identification is performed in several steps, resulting in objects satisfying different reconstruction quality criteria. They can later be used to define different event selections.

Object Preselection

The preselection objects requires to satisfy basic kinematic and reconstruction quality requirements. The objects considered in this analysis are electrons, muons and jets. Electrons and muons are summarized as light leptons. In order to achieve high statistics in signal and control regions, as loose as possible preselection criteria are applied for light leptons.

Electrons with transverse momentum $p_{\mathrm{T}} > 7$ GeV are selected if they satisfy the very loose identification criteria described in Section 4.2. The requirement on the pseudo rapidity measured in the calorimeter and must satisfy $|\eta_{cluster}| < 2.47$. Muons with $p_{\mathrm{T}} > 5$ GeV are selected by the medium identification criteria (c.f. Section 4.2). The pseudo-rapidity must satisfy $|\eta| < 2.7$.

Jets are considered if they have $p_{\mathrm{T}} > 20$ GeV and $|\eta| < 4.9$ with anti-k_{T} radius parameter $\Delta R < 0.4$ (c.f. Section 4.2).

Baseline Objects

Table 5.1: Overlap removal, performed on preselected objects before signal selection in the indicated order.

	Ambiguity	Reconstruction Overlap	Discard
1		e,μ sharing track	e
2	e, jet	$\Delta R(e, \text{jet}) < 0.2$	jet
3		$\Delta R(e, \text{jet}) < 0.4$	e
4	μ, jet	$\Delta R(\mu, \text{jet}) < 0.2$[1]	jet
5		$\Delta R(\mu, \text{jet}) < 0.4$	μ

A particle track may be identified as several different objects by the corresponding reconstruction algorithms. To resolve such ambiguities and of preselected objects have to pass an overlap removal procedure, which objects discards preselected particles according to criteria in the order as indicated in Table 5.1.

Standard Model processes producing heavy quark bound states can result in multileptonic final states. The four-lepton analysis rejects at an early stage leptons originating potentially from leptonic decays of the φ, J/ψ and Υ mesons by so-called "low-mass resonance removal" without loosing to much sensitivity to signal. In the run 1 analysis, the full invariant dilepton mass region below 12 GeV has been rejected. With the keep of more detailed MC simulation, the low dilepton invariant mass region could be investigated in more detail (see Table 5.2).

Both leptons of a pair with opposite charge, because of the danger of misidentified charges, regardless of their flavor, are discarded, if their invariant mass $m(\ell^+, \ell'^-)$ is less than 4 GeV to veto decays of resonances bound states up to the mass of J/ψ meson, $m_{J/\psi}$. The Υ meson decays to same-flavor opposite-sign lepton pairs. That there are no other contributions besides the direct Υ decays above 4 GeV. Therefore an invariant mass cut in a narrow interval around $m_\Upsilon = 9.46$ GeV is applied to same-flavor, opposite-sign lepton pairs. Both leptons are discarded if their invariant mass $m(\ell^+, \ell^-)$ is between 8.4 and 10.4 GeV. The more specific low-mass resonance veto results in an improved sensitivity for low mass neutralinos, compared to run 1.

Reconstructed objects satisfying the above requirements are called "baseline objects" and their are used for the calculation of the missing transverse energy $E_{\mathrm{T}}^{\mathrm{miss}}$ as explained in Section 4.2.

[1] To remove the jet in this overlap removal step it must have either at most one associated tracks from the primary vertex or the muon's momentum is comparable to the jet's momentum. Alternatively to the criterion of an angular separation, the jet is also removed if one of its ID tracks can be matched to the muon.

Table 5.2: Low-mass veto, applied to preselected objects before signal selection

Lepton pair	Invariant mass cut	Discard
$e^+e^-, \mu^+\mu^-, e^\pm\mu^\mp$	$m(\ell^+, \ell'^-) < 4$ GeV	both
$e^+e^-, \mu^+\mu^-$	$8.4 \text{ GeV} < m(\ell^+, \ell^-) < 10.4$ GeV	both

Signal Objects

Only a subset of the baseline objects is considered as signal objects. They have to satisfy further quality, kinematic and/or isolation criteria.

Jets are accepted if $|\eta| < 2.8$ and if they fulfill further conditions to reduce contributions from event pile-up. A jet is considered to be from a pile-up if it has $p_\mathrm{T} < 60$ GeV, $|\eta| < 2.4$ and a JVT score (c.f. Section 4.2) of less than 0.59.

Light leptons must pass cuts on their impact parameter to reduce the effects of non-prompt leptons. Their longitudinal impact parameter must conform to $z_0 \sin\theta < 0.5$ mm. The transversal, normalized to its uncertainty is required to be small; $d_0/\sigma(d_0) < 5$ for electrons and $d_0/\sigma(d_0) < 3$ for muons. Electrons are furthermore required to satisfy the conditions of a tighter identification working point, the "medium" likelihood based identification (c.f. Section 4.2). Both light leptons are required to pass the isolation criterion that is explained in Section 4.3.

Objects satisfying all the aforementioned requirements are referred to as "signal" objects. The complimentary set of baseline objects that did not pass the signal object requirements are given the short-hand name "loose" objects.

5.2 Event Selection

Having assured that the detector is in stable data-taking conditions, events with cosmic muons are vetoed. Muons are discarded as cosmic, if their impact parameters fulfill the conditions

$$z_0 > 1.0 \text{ mm or}$$
$$\text{or } |d_0| > 0.2 \text{ mm.}$$

Moreover, badly measured muons are rejected.

Electrons and muons are used to trigger the event recording (c.f. Section 3.2.5). In this analysis, events are selected using a combination (logical OR) of single lepton, dilepton or trilepton trigger as listed in Table 5.3. Reconstructed signal leptons (c.f. Section 4.2) must also be associated to trigger leptons, which is referred to as "trigger matching". That means the reconstructed object is required to be within $\Delta R < 0.15$ from the relevant trigger object. Reconstructed leptons must then pass an offline p_T threshold. If one of the triggers is prescaled , the next higher unprescaled trigger is used. The trigger efficiency for four-lepton events is close to 100%, using this strategy.

Table 5.3: The triggers and the offline p_T thresholds used in the analysis in 2015 and 2016. Events are used if any of the triggers is passed (logical OR). [20]

Trigger	Offline p_T threshold [GeV]	
	2015	2016
Single isolated e	25	25
Single non-isolated e	61	61
Single isolated μ	21	25
Single non-isolated μ	51	51
Double e	14,14	16,16
Double μ	11,11	11,11 or 15,15
	19,9	21,9
Triple e	18,10,10	18,10,10
Triple μ	19,5,5	21,5,5
	7,7,7	7,7,7
Combined $e\mu$	18(e),15(μ)	18(e),15(μ)
	25(e),9(μ)	25(e),9(μ)
	8(e),25(μ)	8(e),25(μ)
	13(e),13(e),11(μ)	13(e),13(e),11(μ)
	13(e),11(μ),11(μ)	13(e),11(μ),11(μ)

The remaining events are selected if they have at least four light signal leptons in the final state. Leptonically decaying tau leptons are also considered as part of the analysis since they are selected as light leptons.

By means of the so-called effective mass

$$m_{\text{eff}} = \sum_{\ell=e,\mu} p_T(\ell) + \sum_{p_T(j)>40\ \text{GeV}} p_T(j) + E_T^{\text{miss}}, \tag{5.1}$$

which is the sum of the transverse momenta p_T of the objects contributing to the signal signature in an event, the SM background can be distinguished from SUSY signals.

The SM expectation for events with 4 leptons is shown in Figure 5.1. It indicates a better significance in regions with high E_T^{miss} or m_{eff}.

A study was performed to compute the expected significance for different cut values to the m_{eff}, as well as its three components separately. It was found that a cut on the effective mass with $m_{\text{eff}} > 900$ GeV shows the best significance to most of the considered signal models. Nevertheless, a second threshold of 600 GeV was introduced to be also sensitive to other signals than the benchmark model.

Still remaining contributions to the background are mostly originated from one or more Z bosons in an intermediate state. These imply on-shell as well as off-shell

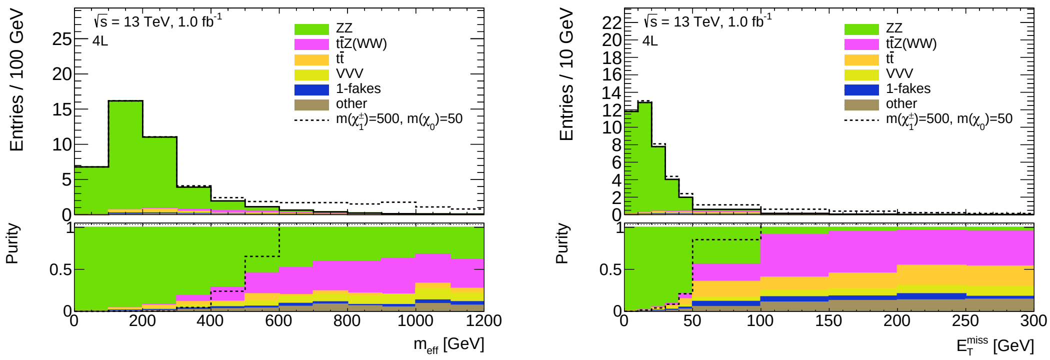

(a) m_{eff} (b) $E_{\mathrm{T}}^{\mathrm{miss}}$

Figure 5.1: The m_{eff} and $E_{\mathrm{T}}^{\mathrm{miss}}$ distributions after the basic four-lepton selection for the main Standard Model backgrounds and a benchmark signal model (dotted line). Purity is defined as the fractional contribution of a process in each bin.

bosons. The invariant mass is a distribution with a peak at the on-shell Z mass $m_Z = 91.2$ GeV. To eliminate most of the backgrounds arising from the SM one applies a Z veto. This Z veto is defined via the invariant mass of the lepton system and fails if any of the following conditions is satisfied[2]:

$$\begin{aligned} |m(\ell^+\ell^-) - m_Z| &< 10 \text{ GeV}, \\ |m(\ell^+\ell^-\ell'^{\pm} - m_Z| &< 10 \text{ GeV}, \\ |m(\ell^+\ell^-\ell'^+\ell'^-) - m_Z| &< 10 \text{ GeV}. \end{aligned} \tag{5.2}$$

Figure 5.2 shows the $E_{\mathrm{T}}^{\mathrm{miss}}$ and m_{eff} distributions of the SM backgrounds and two possible $\chi_1^+\chi_1^-$ signal processes after a Z veto is applied. By this the benchmark signal process has gained in significance, but in return it blinds SUSY scenarios decaying via Z bosons.

To reject the remaining background processes cuts on $E_{\mathrm{T}}^{\mathrm{miss}}$ or the b-jet multiplicity were discussed. Even though they improve the significance to the benchmark model, they would blind the search for alternative SUSY signals. In case of neutrino LSP scenarios the process $pp \rightarrow \tilde{\nu}\tilde{\nu} \rightarrow \ell^+\ell^-\ell^+\ell^-$ might have negligible $E_{\mathrm{T}}^{\mathrm{miss}}$. Furthermore by introduction of a wino-like neutralino $\tilde{\chi}_2^0$, to accompany the NLSP charginos $\chi_1^{\pm}$, b-jets could be produced by the process $\tilde{\chi}_2^0 \rightarrow h\tilde{\chi}_1^0$.

In summary the criteria applied to the events for the first two signal regions in run 2 are given in Table 5.4. It contains furthermore the so-called validation region, VR. It is used to validate the background estimation approaches before looking into data of the signal region. So-called control regions (CR) are defined for each SR as well as the VR. They select loose leptons (c.f. Section 5.1) for data-driven background estimation as discussed in detail in Chapter 6.

[2] ℓ' may or may not have the same flavour as ℓ

Table 5.4: Signal regions (SR), validation region (VR) and control regions (CR) definitions for the four-lepton analysis [20]

Sample	$N(e,\mu)$ signal	Z boson	m_{eff} [GeV]	
SRA	$>= 4$	$>= 0$	veto	> 600
CR-SRA	$= 2$	$>= 2$	veto	> 600
SRB	$>= 4$	$>= 0$	veto	> 900
CR-SRB	$= 2$	$>= 2$	veto	> 900
VR	$>= 4$	$>= 0$	veto	< 600
CR-VR	$= 2$	$>= 2$	veto	< 600

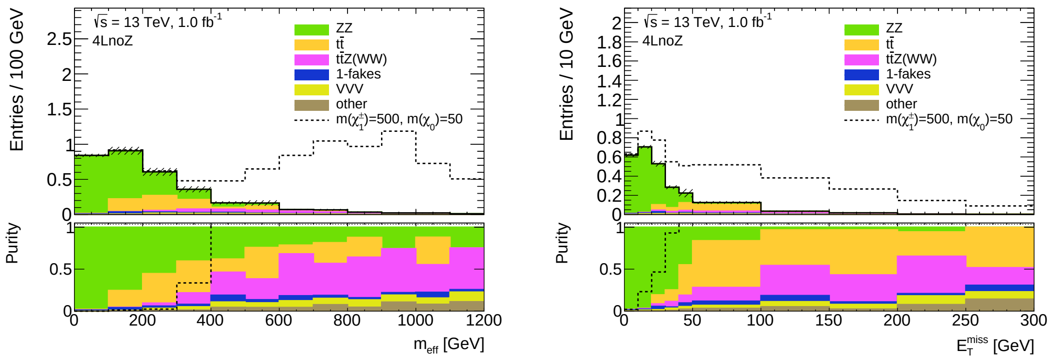

(a) m_{eff} (Z veto)

(b) $E_{\text{T}}^{\text{miss}}$ (Z veto)

Figure 5.2: m_{eff} and $E_{\text{T}}^{\text{miss}}$ distributions to the main Standard Model backgrounds, in events with $\geqslant 4$ light leptons after the additional Z veto (Normatization for 1.0 fb^{-1}).

5.3 Background Expectation

To get the best possible significance for an exclusion as well as for a discovery, the estimation of the expected background must be as precise as possible. The increase of center-of-mass energy from 8 to 13 TeV does not only increase the cross section of possible signal processes but also those of the background. The next sections introduce qualitatively the main sources of backgrounds. They can be subdivided into reducible background and irreducible background depending on the mechanism that leads to it.

5.3.1 Irreducible background

Irreducible background consists of processes that have exactly the same signature as the signal, meaning the prompt production of four or more real leptons in the primary vertex. They are considered as prompt, if the life time of intermediate particles is shorter than about 1 ps. This results in a flight length of less than 300 μm . The detector is not able resolve the displacing of the vertex. This kind of

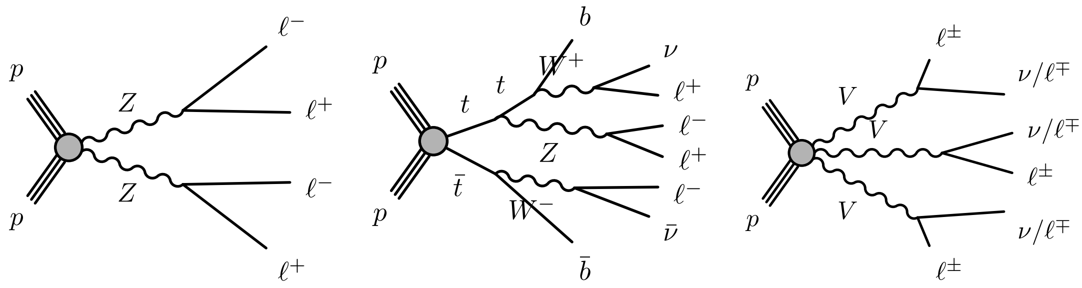

Figure 5.3: Main SM background processes with at least 4 real leptons in the final state ($V = W, Z$).

detected events look exactly like the wanted signal and cannot be removed by the signal objects definitions.

In the four-lepton event selection, described in Section 5.2, the main sources for irreducible background are from the rare top-quark pair production in association with a Z boson ($t\bar{t}Z$), or the simultaneous production of two (ZZ) or three (ZZZ,ZZW,ZWW) vector bosons. These processes are depicted in Figure 5.3.

Although there is a Z veto applied that removes the majority of process with Z bosons nearly all irreducible background processes in the four-lepton event selection (c.f. Section 5.2) still contain at least one Z-boson. These Z-bosons are usually virtual.

The dominant source for irreducible background, with a background fraction of more than 40%, results from the rare top-quark pair production in association with a Z boson ($t\bar{t}Z$). It yields four prompt light leptons only if both top quarks as well as the Z boson decay exclusively to (charged) leptons. Which happens with a decay branching ratio of $\frac{1}{9} \times \frac{1}{9} \times 0.033$. The simultaneous production of two Z-bosons (ZZ) still yields a contribution of 20% to the irreducible background. Some other vector boson production processes summarized as triboson processes ($VVV = ZZZ, ZZW, ZWW$) may result in four or more prompt leptons and still have a fractional contribution of about 10%, which is as much as the Higgs decay contribution.

5.3.2 Reducible Background

Reducible background consists of less than four signal objects from the primary vertex interaction, referred to as the *hard process*. Missing leptons, required for a four lepton event selection, are produced in secondary processes or are the result of misreconstructions. For convenience, they are referred to as fake leptons, although they might be real leptons (but not prompt).

The mechanism happening subsequently to the hard process is referred to as *soft process* and distinguishes the following three fake types:

Heavy flavor leptons (HF), that arise from the semileptonic decay of heavy hadrons, which contain c-or b-quarks. It is found (see figure 6.3) that this source is the dominant one for fake leptons in four-lepton events. It will have a detailed discussion in Chapter 6.

Light flavor leptons (LF) arise from light hadrons including those containing strange quarks. For electrons, this is usually a misidentified charged pion or kauon. The LF muons can be produced in many ways for example a decaying pion. Light flavor decays play a sub-dominant role for muons and almost no role for electrons in this analysis.

Conversion electrons (CO) are produced by γ's in the detectors material. Usually, the γ itself is produced via bremsstrahlung. In the energy regions within the ATLAS-detector the by far most dominant mechanism is the e^+e^- pair production. It is negligible for muons.

In total, the fraction of reducible background is about 10 to 15%.

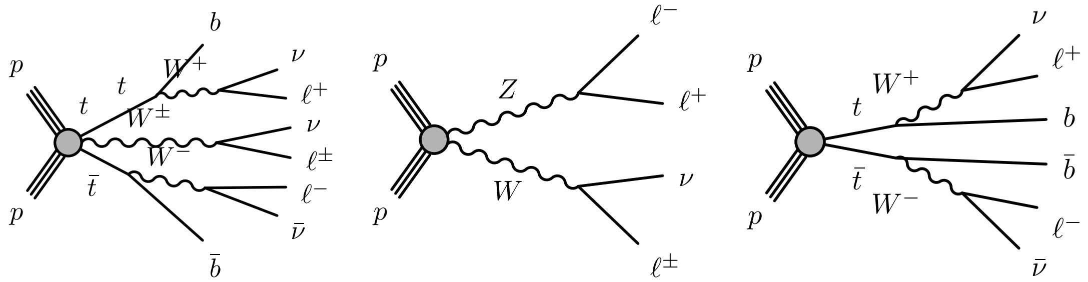

Figure 5.4: Leading reducible background sources

The reducible background is further distinguished according to the number of fake leptons required to match the selection:

1-Fake Processes are those reducible processes that require at least one fake lepton. The processes $gg \to t\bar{t}^* \to t\bar{t}W$ and $q\bar{q}' \to W^{(*)}Z^{(*)}$ as depicted in Figure 5.4(a) and 5.4(b) contribute with 45% to the total reducible background.

2-Fake Processes are accordingly four-lepton processes with two real leptons and at least two fake leptons. It turned out that top-quark pair production, shown in Figure 5.4(c), is the only such process contributing to the signal regions. The production of a single Z-boson with associated QCD radiation as recoil is called Z+jets. Based on MC simulation, it does not play a role in the four-lepton signal region, because its average m_{eff} is quite low. Nevertheless, it plays an important role in the region below the m_{eff} cuts and hence for the validation of the background estimation.

Reducible backgrounds with **three or more fakes** were found to be negligible in the four-lepton analysis.

5.3.3 MC Simulation of the Background

As a first approach all expected backgrounds are estimated using MC simulations. The samples used for background estimation are listed in Table 5.6.

The total yields for each separate sample in the signal regions as well as in the validation region are listed in Table 5.5.

The production of these samples are typically a very demanding process in terms of computing resources and executing time. Therefore the number of simulated events are partially limited, resulting in statistic uncertainties. This can be observed especially for the 2-fake processes, $t\bar{t}$ and $Z + jets$. The uncertainties in the signal regions are about 100%. The sample $\mathbb{Z} + jets$ does not have any simulated signal events.

Furthermore simulation based background estimation is affected by multiple systematic uncertainties resulting either from experimental or theoretical sources. Theoretical uncertainties come from the determination of the cross-section and from the choice of the MC generator. This is typically of the order of 10%. Experimental uncertainties arise due to several factors of similar size totalling to about 10%. These are, for example, lepton identification efficiencies, energy scales and uncertainties on the luminosity. The systematic uncertainty associated with the simulation of pile-up is also taken into account.

The background estimation of irreducible background and 1-fake background completely relies on MC yet. In contrast, an alternative was developed to estimate the reducible 2-fake processes by a data-driven approach which is discussed in Chapter 6.

Table 5.5: Expected yields for 13.3 fb^{-1} in the four-lepton validation and signal regions. Statistical and systematic uncertainties are included.

Sample	VR	SRA	SRB
Irreducible			
ZZ	29 ± 5	0.6 ± 0.4	0.20 ± 0.19
Z	2.05 ± 0.24	1.43 ± 0.23	0.47 ± 0.09
Higgs	1.7 ± 1.4	0.4 ± 0.4	0.11 ± 0.11
VVZ	0.72 ± 0.14	0.31 ± 0.06	0.123 ± 0.027
Others	0.28 ± 0.07	0.32 ± 0.04	0.181 ± 0.022
1-fake			
WZ	0.89 ± 0.07	0.074 ± 0.015	0.033 ± 0.013
$t\bar{t}W$	0.240 ± 0.020	0.092 ± 0.010	0.035 ± 0.004
2-fake			
Z+jets	15.8 ± 6.3	0 ± 0	0 ± 0
$t\bar{t}$	7.2 ± 2.7	0.32 ± 0.16	0.061 ± 0.068

Table 5.6: Simulated SM background samples used for the background estimation ($V = W, Z$).

Process	Generator(s)	Cross-section	UE tune calculation	PDF set
$t\bar{t}Z$, $t\bar{t}W$, $t\bar{t}WW$	MadGraph 5_aMC@NLO [34] + Pythia 8 [29]	NLO	A14	NNPDF23LO
tWZ	aMC@NLO [48] + Pythia 8	NLO	A14	NNPDF23LO
ZZ, WZ, WW	Powheg [33] + Pythia 8	NLO	AZNLO	CTEQ6L1
$t\bar{t}$	Powheg + Pythia 6 [49]	NNLO+NNLL	Perugia2012	CT10
Z+jets, W+jets	MadGraph 5_aMC@NLO	NNLO	A14	NNPDF23LO
Higgs (ggF, VH, VBF H) $t\bar{t}$H	Powheg + Pythia 8 aMC@NLO + Pythia 8	NNLO+NNLL NLO	Perugia2012 UE EE5	CT10 CTEQ6L1 (CT10ME)
VVV	Sherpa	NLO	Default	CT10
$tt\bar{t}$, $t\bar{t}t\bar{t}$	MadGraph 5_aMC@NLO + Pythia 8	NLO	A14	NNPDF23LO

Chapter 6

Data-Driven Background Estimation

Fake factor studies were already performed in the analysis performed in run 1 [16]. This chapter follows by parts discriptions in the corresponding support note as well the support note if [20], to which I have contributed to.

6.1 Concept

Necessity of Data-Driven Background Estimation

The estimations of SM backgrounds in Figures 5.2, are from MC simulation. But MC-based estimations are affected by statistical and systematic uncertainties. The production of MC samples for small background contributions with adequate statistics is very demanding in terms of computing resources and execution time.

For the $t\bar{t}$ process, for example, there is only $\mathcal{O}(1)$ simulated event in the signal regions. Furthermore MC simulation is subject to theoretical and experimental uncertainties (c.f. Section 5.3.3).

Data driven background estimation techniques use signal-depleted data samples for the determination of reducible background yields avoids systematic uncertainties mentioned above and providing better statistics. A data-driven method called the fake factor (FF) method is used for the determination of reducible backgrounds with two fake leptons (2-fake background) in this analysis. The following describes the concept and application, Sections 6.2 and 6.3 discuss the determination of the fake factor using MC. To maintain a fully data-driven approach, a correction factor to the FF from data is determined in Section 6.4.

Matrix Method

A general method of data-driven background estimation is the so-called Matrix- or ABCD-method. It estimates background yields from data in selected regions

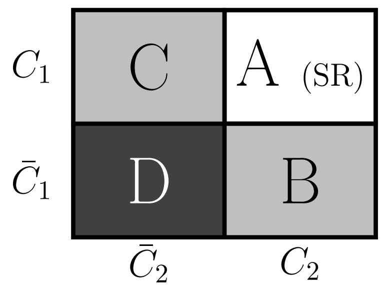

Figure 6.1: Illustration of the ABCD method. It estimates the background yields in a signal region A using data. A is selected by at least two independent criteria C_1 and C_2. Regions B and C are selected by inverting either one of that criteria, whereas for region D both criteria are inverted ($\bar{C}_1$ and $\bar{C}_2$).

disjunct from the actual signal region called control regions (CR) by extrapolating to the signal region (SR). The control regions are distinguished from the signal region by inverting one or more signal selection criteria as illustrated in Figure 6.1. These criteria have to be statistically uncorrelated. They discriminate the signal from the background such that the background occurs in SR and CR, but the signal process only in SR.

Measurement in the control regions, B, C and D allows for estimation of the contribution in the signal region A by scaling the event yields in the control regions: of the background using

$$N_\mathrm{A} = \frac{N_\mathrm{B}}{N_\mathrm{D}} \cdot N_\mathrm{C} = \frac{N_\mathrm{C}}{N_\mathrm{D}} \cdot N_\mathrm{B}.$$

Fake Factor Method

To distinguish between reducible background containing misidentified objects and signal events, the fake factor method makes use of differences in object characteristics between prompt and fake leptons on a statistical basis. Fake leptons are more likely to be rejected by the signal object requirements than prompt leptons. Leptons are first classified as “loose” (l) or “signal” (L) leptons according to their reconstruction quality as defined in Section 5.1. The ratio

$$F = \frac{f_\mathrm{signal}}{f_\mathrm{loose}} \tag{6.1}$$

defines the fake factor, where f_signal (f_loose) is the probability that a fake lepton is misidentified as a signal (loose) lepton and $f_\mathrm{signal} + f_\mathrm{loose} = 1$. Instead of determining this extrapolation factor in one step, as it is done in the ABCD method, the fake factor is determined in several steps which are discussed in the following sections.

Two CRs are defined for each SR differing from it only in the quality of the reconstructed leptons. The first control region, CR1, uses a 3L1l selection, requiring exactly three signal leptons and at least one loose lepton with a corresponding fake factor F. The second control region, CR2, is defined by a 2L2l selection, requiring exactly two tight leptons and at least two loose leptons with two corresponding fake factors F_1 and F_2 which do not need to be the same. The number of reducible background events in the signal region, $N_{\text{red}}^{\text{SR}}$, can be determined from the numbers of events in the two data CR, $N_{\text{data}}^{\text{CR1}}$ and $N_{\text{data}}^{\text{CR2}}$, using

$$N_{\text{red}}^{\text{SR}} = (N_{\text{data}}^{\text{CR1}} - N_{\text{irr, MC}}^{\text{CR1}}) \cdot F^{\text{CR1}} - (N_{\text{data}}^{\text{CR2}} - N_{\text{irr,MC}}^{\text{CR2}}) \cdot F_1^{\text{CR2}} F_2^{\text{CR2}}. \tag{6.2}$$

The first term accounts for all reducible background events, including the 1-fake as well as the 2-fake events. Since 2-fake processes have two fake leptons they are double counted in CR1. The second term subtracts the double counting using CR2. In each control region, the contribution from irreducible background ($N_{\text{irr, MC}}^{\text{CRX}}$) is subtracted from the data using MC simulation.

For the reducible background in four-lepton signal regions, this general approach can be simplified: The hard process contributions in CR1 and CR2 are estimated using MC as explained in Section 5.3. Figure 6.2 shows the yields of a selection as for CR1 and CR2, but without the m_{eff} cut, as a function of m_{eff}. It indicates rather low statistics in CR1 compared to CR2. Furthermore, CR1 suffers from a substantial contamination by irreducible background. Its application for background estimation, therefore, results in large uncertainties. On the other hand, CR2 does not suffer from contamination by irreducible backgrounds. The main purpose of CR1 is to estimate the reducible background of 1-fake processes, whereas 2-fakes can be estimated using both, CR1 and CR2.

CR1 is dominated by processes with two fake leptons ($t\bar{t}$) or irreducible background, rather than the expected 1-fake processes (WZ and $t\bar{t}W$). If the general FF method were used, it would essentially only take into account the 2-fake processes twice using CR1 and then a third time using CR2.

Therefore the general FF method, Formula (6.2), is simplified for the four lepton analysis using only the pure and high statistics control region CR2:

$$N_{\text{red}}^{\text{SR}} = (N_{\text{red}}^{\text{CR2}} - N_{\text{irr}}^{\text{CR2}}) \cdot F_1^{\text{SR}} \; F_2^{\text{SR}}. \tag{6.3}$$

However, it has to be taken into account that 1-fake processes are not considered in this data-driven estimation and have to be estimated by MC.

The fake factor depends on the lepton flavor and depends on transverse momentum (p_{T}) and pseudo rapidity (η). It also depends strongly on the soft process producing fake lepton (c.f. Section 5.3.2) and on the hard process. As a consequence, fake factors obtained from a control region in data are not directly applicable to CR1 and CR2, where the composition of soft and hard processes are significantly different. Therefore, in this analysis the fake factors are obtained for each process separately from MC simulated samples and are corrected with a soft

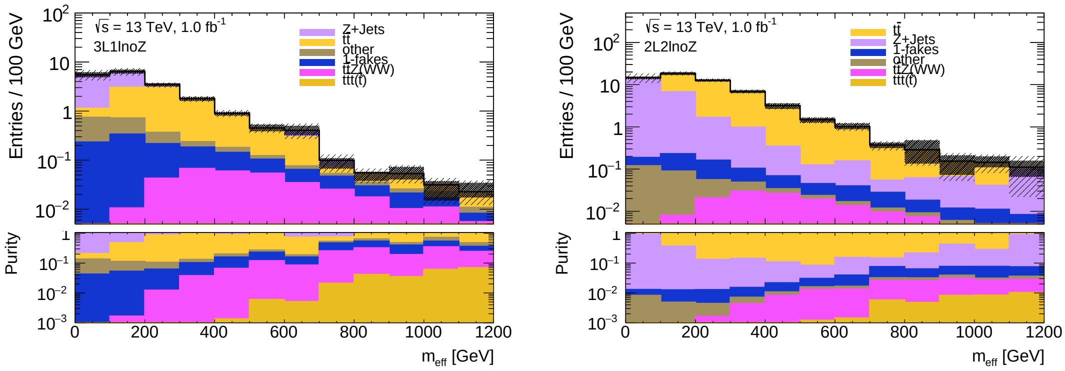

(a)

(b)

Figure 6.2: Yields and fractional composition of background processes in the control regions CR1 (a) and CR2 (b) as a function of m_{eff} with m_{eff} cut is omitted.

process dependent scale factor sf to account for differences between data and MC simulation. The corrected fake factors F^{ij} for each combination of hard process j (e.g. top-quark pair production) and soft process i (HF,LF,CO; c.f. Section 5.3.2) then are combined to a so-called "weighted average fake factor":

$$F_{\mathrm{SR}} = \sum_{i,j} \left(R^{ij}_{\mathrm{SR}} \cdot sf^{i} F^{ij} \right) . \tag{6.4}$$

Where the sf_i is assumed to be independent of the hard process. The weight R^{ij}_{SR} is called the process fraction.

6.2 Process Compositions

To obtain the weighted average FF according to Formula (6.4), it is necessary to determine the process fractions R expected in the CRs. With the simplification discussed in Section 6.1, the only remaining non-negligible hard process which is estimated by the FF method is the $t\bar{t}$ process[1]. Since the FFs are quite different for the different soft processes, their contribution to the $t\bar{t}$ background must be determined.

Figure 6.3 shows the contributions of heavy flavor (HF), light flavor (LF) and conversion (CO) fakes as a function of p_{T} and $|\eta|$ in a simulated $t\bar{t}$ sample. The fake types are determined using truth information (c.f. Section 4.1). The figure indicates the relative importance of the HF fakes. The with more than 90% vast majority of fake leptons in the $t\bar{t}$ sample is due to HF. Uncertainties in this contribution have the largest impact on the weighted average FF and its systematic uncertainty. Therefore the HF FF is determined especially precisely in Section 6.4.

[1] For validation of this approach an investigation similar to the $t\bar{t}$ is needed for $Z + jets$. This has also been studied in [20].

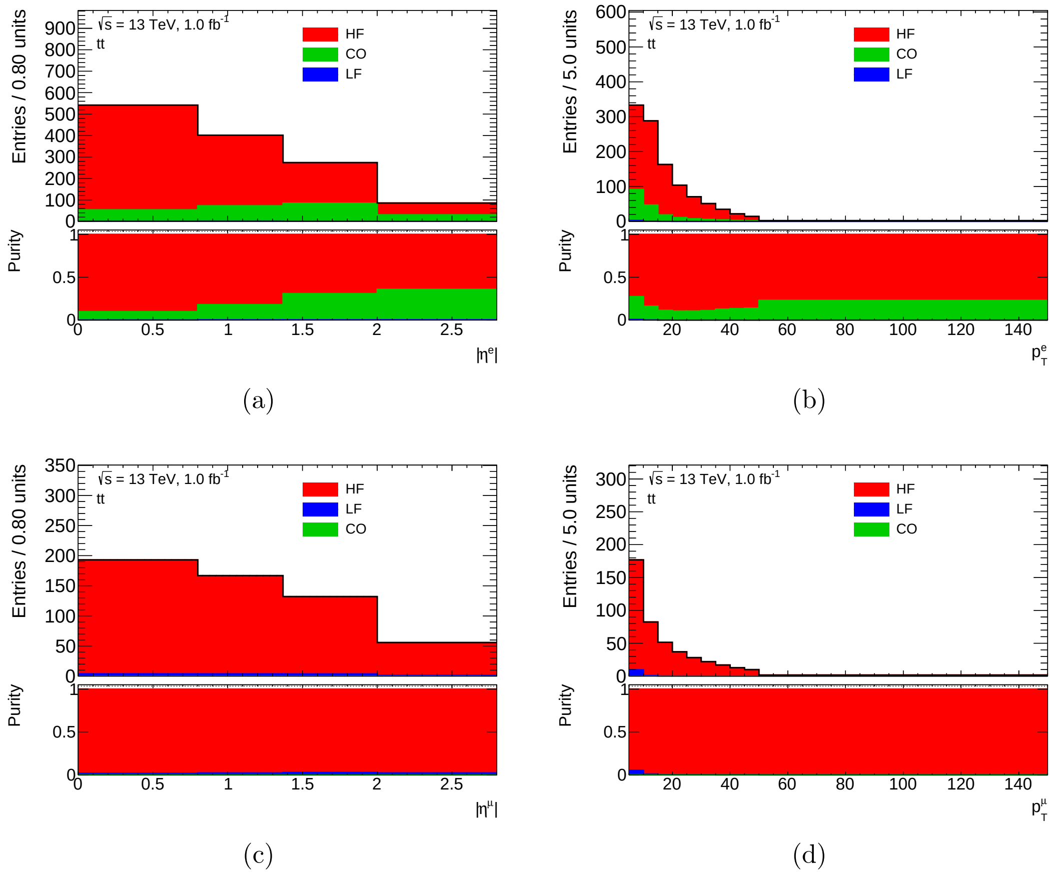

Figure 6.3: p_T- and η-dependent contributions of fake electrons (a,b) and muons (c,d) of different sources in a $t\bar{t}$ sample using truth information (heavy flavor (HF), light flavor (LF) and conversion (CO) fake leptons).

6.3 Fake Factors in Monte Carlo

After the determination of the process fractions in the SR, the next step is to compute the FFs in MC. The truth classification (c.f. Section 4.1) allows for determining the origin of each lepton (prompt, HF, LF or CO).

To obtain a FF appropriate for the control and signal regions, the selection has to be as close as possible to the CR2 selection. On the other hand, it has already been observed that the MC statistics after the four-lepton selection is not sufficient to predict the FF reliably. It is assumed, that the appearance of multiple fake leptons within one event is uncorrelated. This was confirmed by comparing the averaged FF for a four-lepton selection with the ones for looser selections which agreed within statistical uncertainties. In contrast, a fully hadronic decay of one or both top quarks would produce light jets which can influence the HF fake factor measurement. Therefore, it is required that both top quarks decay semi-leptonically and the decay leptons are classified as prompt.

The FF turns out to depend only weakly on the m_{eff} cut. While they do not always precisely match, the control region composition is sufficiently close to the signal region composition. Even $\mathcal{O}(100\%)$ uncertainties on the estimation of fake light lepton yields are tolerable as was the case in the search at $\sqrt{s} = 8$ TeV. To maximise statistics, the fake factor measurement in simulated $t\bar{t}$ events is done in a selection with 2 prompt leptons and arbitrary many fake leptons without m_{eff} requirement.

The FFs are determined from numbers of fake leptons according to N^i_{signal} and N^i_{loose},

$$F^i(p_{\text{T}}, \eta) = \frac{f^i_{\text{signal}}(p_{\text{T}}, \eta)}{f^i_{\text{loose}}(p_{\text{T}}, \eta)} = \frac{\frac{N^i_{\text{signal}}(p_{\text{T}},\eta)}{N^i(p_{\text{T}},\eta)}}{\frac{N^i_{\text{loose}}(p_{\text{T}},\eta)}{N^i(p_{\text{T}},\eta)}} = \frac{N^i_{\text{signal}}(p_{\text{T}}, \eta)}{N^i_{\text{loose}}(p_{\text{T}}, \eta)} \tag{6.5}$$

for only one hard background process ($t\bar{t}$), and

$$F_{\text{SR}}(p_{\text{T}}, \eta) = \sum_i R^i_{\text{SR}} sf^i F^i(p_{\text{T}}, \eta) \tag{6.6}$$

where the index i distinguishes the soft processes, HF, LF or CO, leading to a fake lepton and N^i is the total number of loose and signal leptons from each soft process.

It turned out that the FFs have a significant dependence only on p_{T} and η and no other event variables jet multiplicity, m_{eff} and $E_{\text{T}}^{\text{miss}}$ which have been tested.

The scale factor sf for the HF process is determined from data in Section 6.4.

6.3.1 CO Fake Factor

Conversions only play a role for electrons. The overall FF is quite small thanks to the high rejection rate of the reconstruction algorithms. The criteria for baseline and, thus, loose leptons (c.f. Section 5.1), are also chosen such that the FF stays small. A small FF is important for a small statistical uncertainty when extrapolating from CR to SR.

The results for the FF as a function of p_{T}, $|\eta|$, $E_{\mathrm{T}}^{\mathrm{miss}}$, m_{eff} and jet multiplicity are shown in Figure 6.4. The FF raises slightly with p_{T}, from 0.025 to 0.06. It increases with $|\eta|$ from 0.028 in the barrel up to 0.045 in the end caps of the detector.

The average CO FF for electrons is found to be

$$F_{t\bar{t},\mathrm{CO}}^{(e)} = 0.0327 \pm 0.001(\mathrm{stat}).$$

6.3.2 LF Fake Factor

The LF fake contribution is small and negligible for electrons. Figure 6.5 shows its sharp rise to 0.4 for low-energy muons with $p_{\mathrm{T}} < 20$ GeV. It vanishes completely for p_{T} values greater than about 30 GeV. The LF FF is nearly independent of $|\eta|$ and the average value is:

$$F_{t\bar{t},\mathrm{LF}}^{(\mu)} = 0.345 \pm 0.012(\mathrm{stat}).$$

6.3.3 HF Fake Factor

The most important fake contribution is caused by heavy flavor jets (see Figures 6.6 and 6.7 for muons and electrons, respectively). The main dependence of the muon FF is on p_{T}, shrinking down from 0.4 for soft leptons to a value of less than 0.01 for high-p_{T} muons with $p_{\mathrm{T}} > 50$ GeV. The electron FF is again small, compared to the muon FF. It is also strongly p_{T}-dependent and reaches a maximum value of 0.16 at low electron energies.

For both light lepton flavors, the FF in the end caps is about twice as high as in the barrel region. The average values are:

$$F_{t\bar{t},\mathrm{HF}}^{(e)} = 0.107 \pm 0.001(\mathrm{stat}),$$
$$F_{t\bar{t},\mathrm{HF}}^{(\mu)} = 0.234 \pm 0.001(\mathrm{stat}).$$

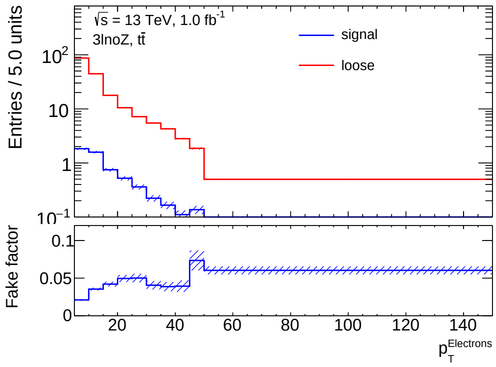

(a) p_{T}

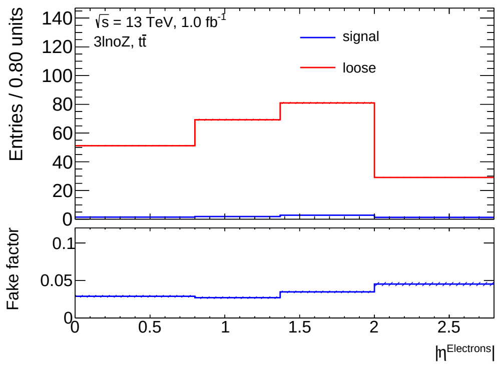

(b) η

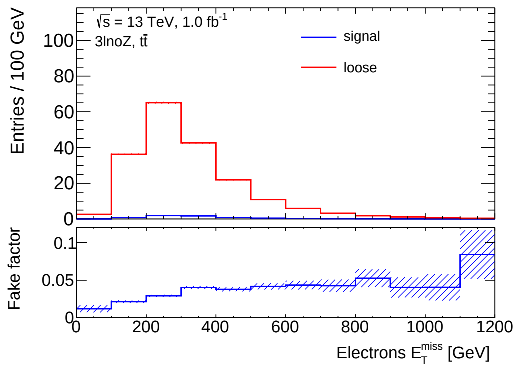

(c) m_{eff}

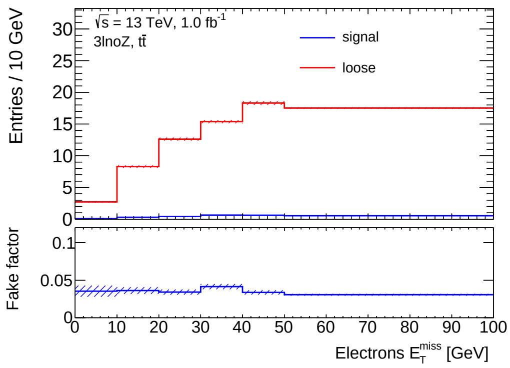

(d) $E_{\mathrm{T}}^{\mathrm{miss}}$

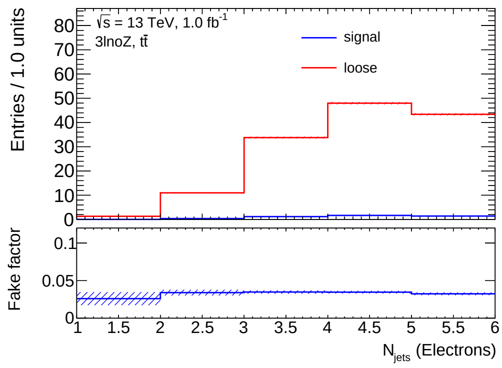

(e) # jets

Figure 6.4: The **CO Fake Factor for electrons**. The upper panels show the total yields for signal (red) and loose (blue) electrons arising from conversion and the lower panels the FF as a function of electron p_{T} and η as well as m_{eff}, $E_{\mathrm{T}}^{\mathrm{miss}}$ and the jet multiplicity of the events. The dashed areas indicate the statistical uncertainties.

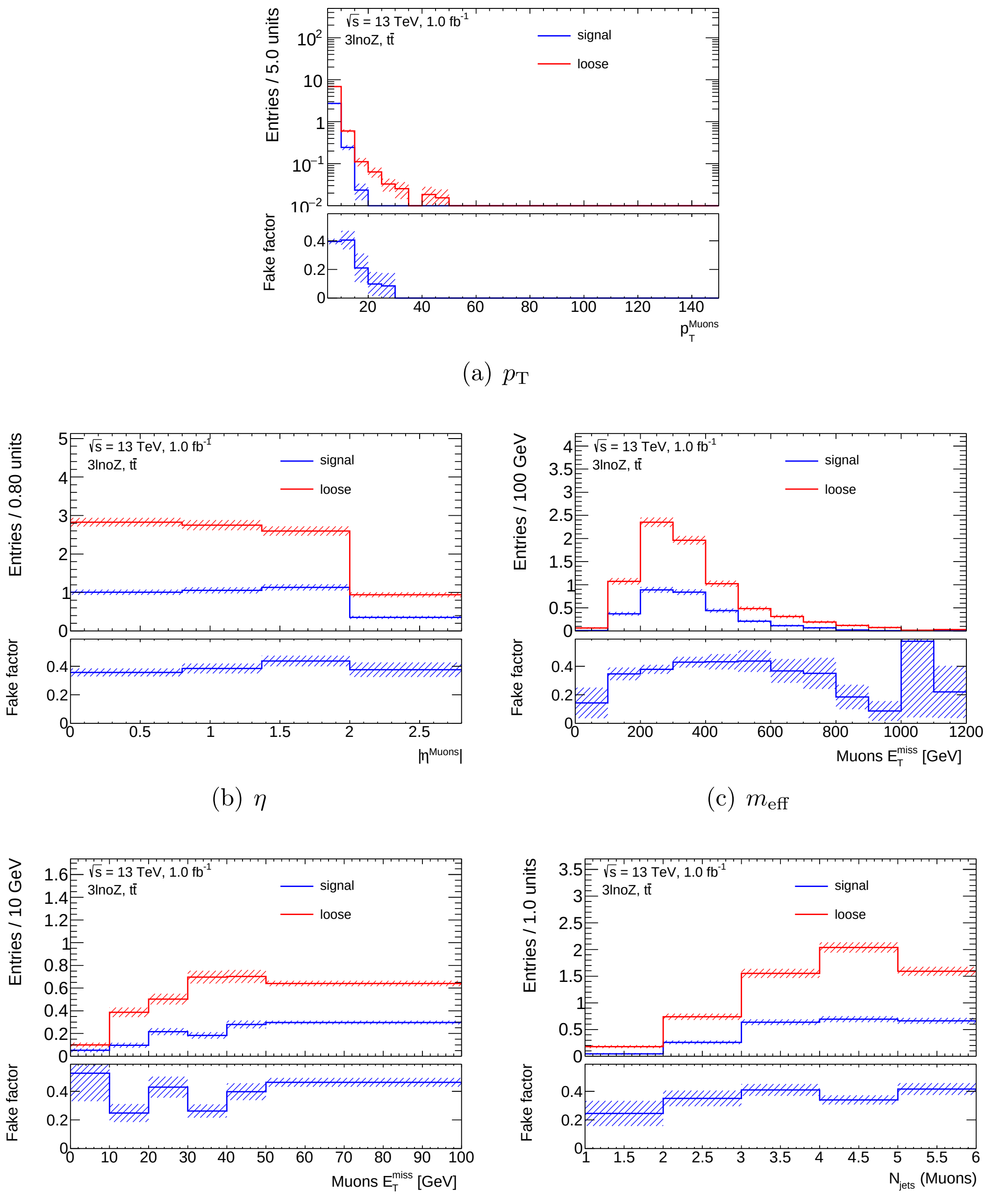

(a) p_{T}

(b) η

(c) m_{eff}

(d) $E_{\mathrm{T}}^{\mathrm{miss}}$

(e) # jets

Figure 6.5: The **LF Fake Factor for muon**. The upper panels show the total yields for signal (red) and loose (blue) muons arising from decaying light mesons and the lower panels the FF as a function of muon p_{T} and η as well as m_{eff}, $E_{\mathrm{T}}^{\mathrm{miss}}$ and the jet multiplicity of the events. The dashed areas indicate the statistical uncertainties.

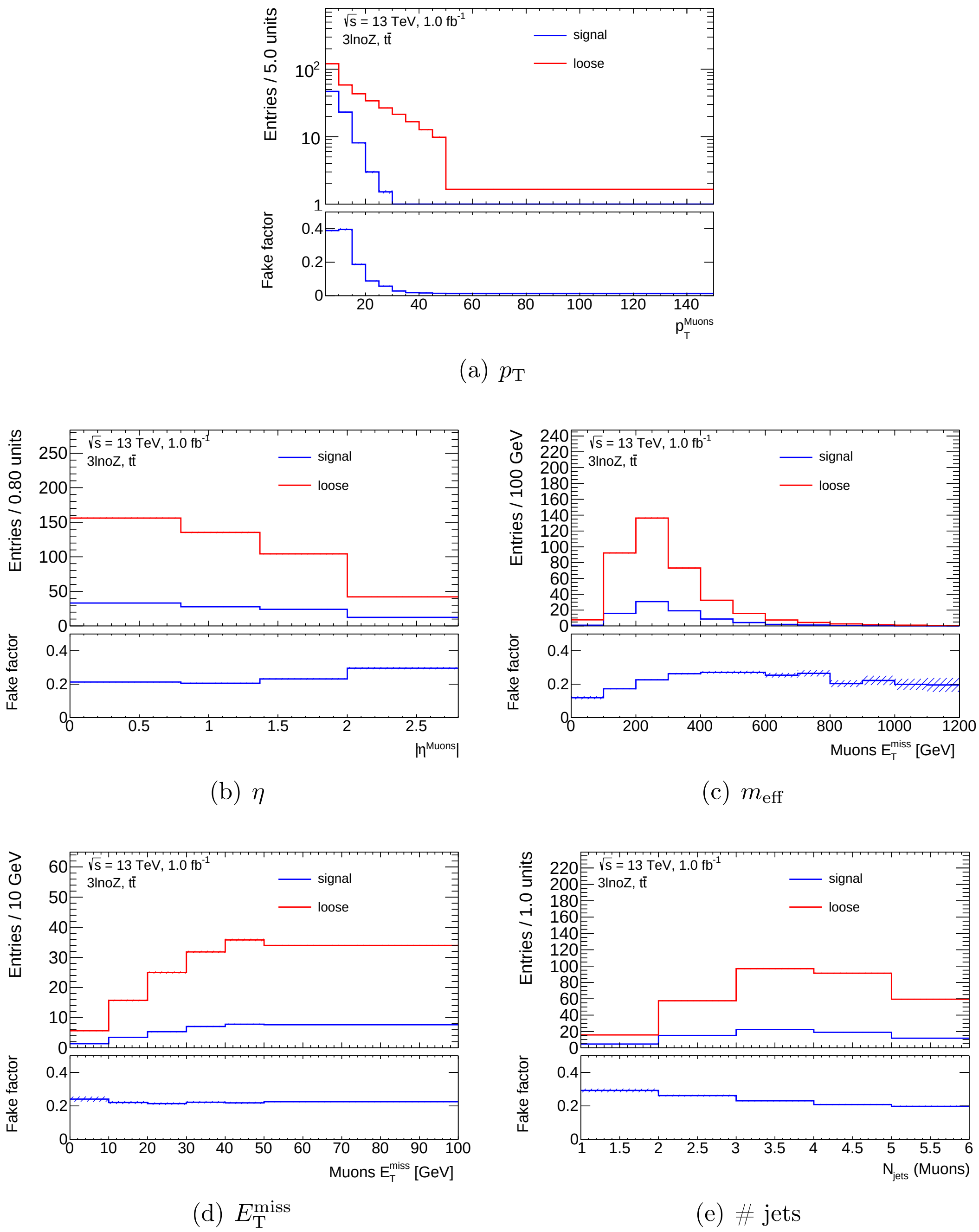

(a) p_{T}

(b) η

(c) m_{eff}

(d) $E_{\mathrm{T}}^{\mathrm{miss}}$

(e) # jets

Figure 6.6: The **HF Fake Factor for muons**. The upper panels show the total yields for signal (red) and loose (blue) muons arising from heavy flavor hadron decays and the lower panels the FF as a function of muon p_{T} and η as well as m_{eff}, $E_{\mathrm{T}}^{\mathrm{miss}}$ and the jet multiplicity of the events. The dashed areas indicate the statistical uncertainties.

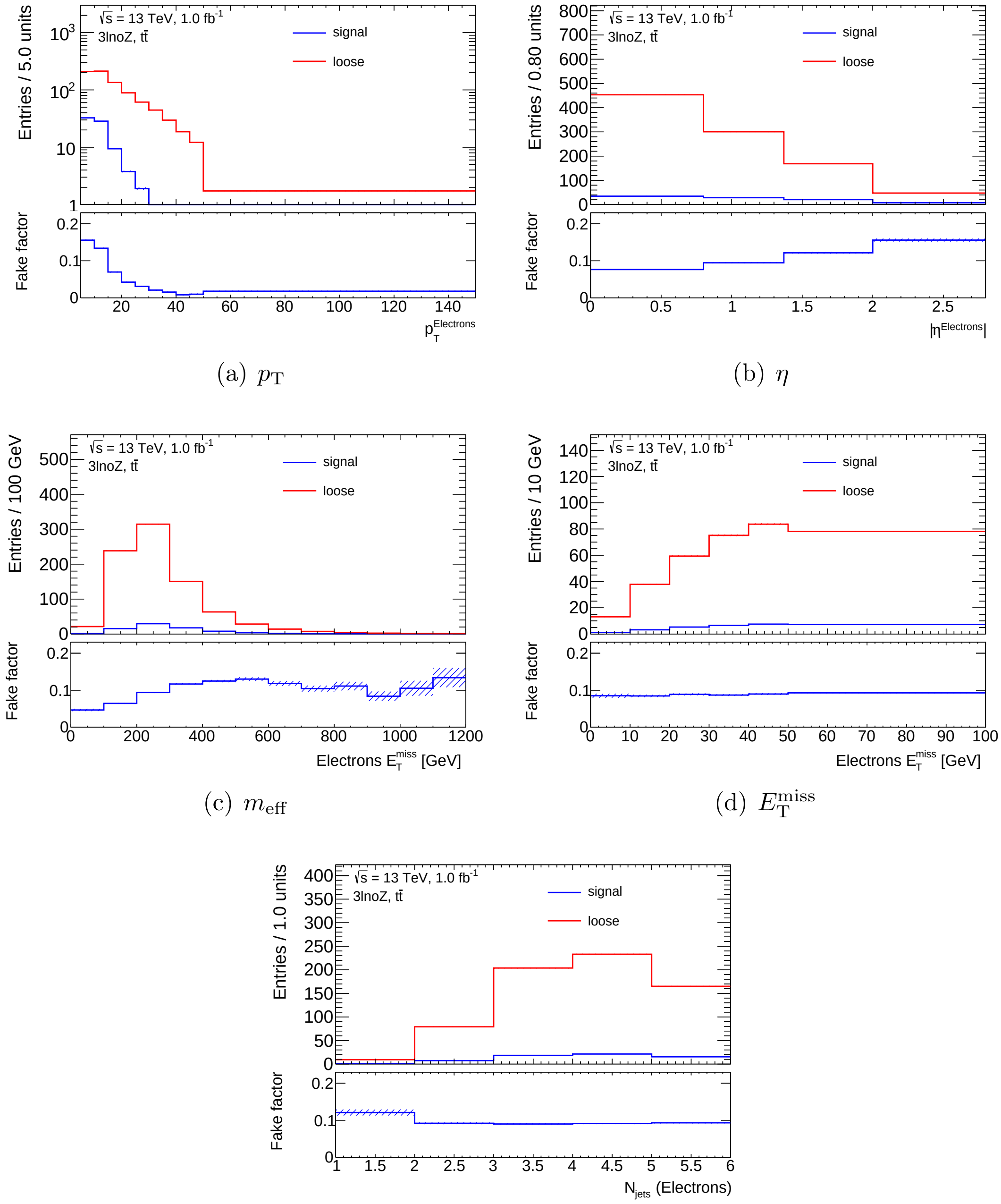

(a) p_{T}

(b) η

(c) m_{eff}

(d) $E_{\mathrm{T}}^{\mathrm{miss}}$

(e) # jets

Figure 6.7: The **HF Fake Factor for electrons**. The upper panels show the total yields for signal (red) and loose (blue) electrons arising from heavy flavor hadron decays and the lower panels the FF as a function of electron p_{T} and η as well as m_{eff}, $E_{\mathrm{T}}^{\mathrm{miss}}$ and the jet multiplicity of the events. The dashed areas indicate the statistical uncertainties.

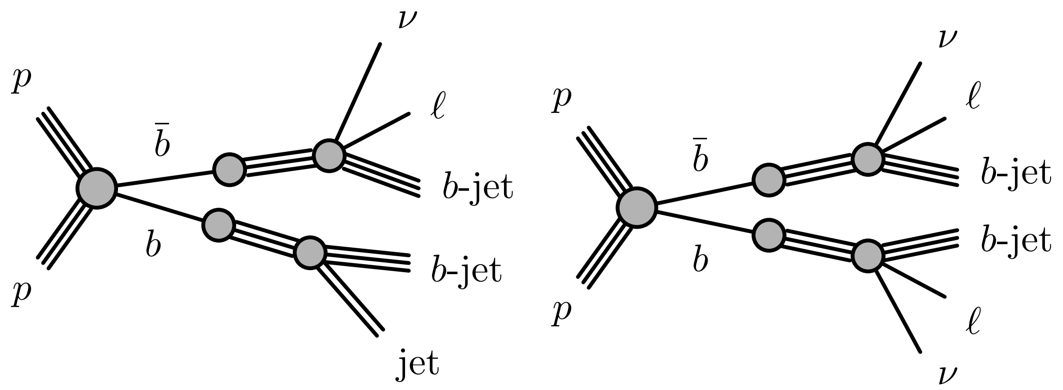

Figure 6.8: $b\bar{b}$ production process with semi-leptonic decays of the b-hadrons in the b-jets.

6.4 Data-Driven Correction: The Scale Factor

In a fully data-driven background estimation, the FF itself is determined from data. A direct measurement of the HF leptons in $t\bar{t}$ events is quite difficult, but has been attempt in Section 6.5.

As a first approach the FFs are determined from Monte Carlo simulated events. To account for differences between data and simulation, corrections with scale factors (sf) are applied. They are supposed to correct for mismodelling of the soft processes HF, CO and LF. Because the HF FF is the dominant contribution to the overall FF, its determination is described first in this Section.

The fake factors differ completely with the selections, in particular if it selects different hard processes. For example, the fake factor for HF leptons in top decays is smaller than the factor for HF leptons in W/Z(+jets) events due to the harder b-quark momentum spectrum in top decays. For a HF lepton with given p_{T}, a low-energetic b-quark has less energy left to transfer to the remaining hadronic decay products. Thus the hadronic activities around the lepton are reduced, making the lepton pass the isolation criteria more easily and leading to a higher fake factor.

The fake factors from MC simulation are regarded here as first order approximation, and the data-driven correction with the scale factor, sf, as second order correction. The scale factor is assumed to be independent of the hard process and applicable to all HF fake factors.

The heavy flavour scale factor, sf^{HF}, is the ratio of the HF fake factors in data and in simulation. It is determined using a so-called tag-and-probe method following a similar approach as in run 1.

6.4.1 Tag-and-Probe Method

The goal of the tag-and-probe method is to determine the HF fake factors in data and MC. The HF scale factor used in this analysis is measured in a $b\bar{b}$ and $c\bar{c}$ enriched region. It is the ratio

$$sf^{HF} = \frac{F^{\text{data}}_{b\bar{b},\text{HF}}}{F^{\text{MC}}_{b\bar{b},\text{HF}}}, \tag{6.7}$$

where $F^{\text{data}}_{b\bar{b},\text{HF}}$ and $F^{\text{MC}}_{b\bar{b},\text{HF}}$ are the fake factors measured in this region in data and in MC, respectively. The leptons in the $pp \to b\bar{b}$ ($pp \to c\bar{c}$) sample (see Figure 6.8) are almost pure HF.

The basic idea of the method is that one of the two semi-leptonic b (c) decays $b\bar{b}$ ($c\bar{c}$) process serves as the tag indicating that it is indeed a $b\bar{b}$ ($c\bar{c}$) event, the other as probe used for the fake probability determination (c.f. Figure 6.8). A jet trigger, which usually has a high p_{T} threshold would limit the probes to similar high p_{T} due to correlation with the jet p_{T}. As has been shown in Section 6.3.3, the largest fake contributions are at low lepton p_{T}, which makes jets an inadequate choice for a tag. The solution is to use a secondary particle within the jet, a muon from semi-leptonic b-quark decay. It does not pass the overlap removal and is thus no baseline object and in particular not a fake lepton, but can be used as a tag.

The tag is chosen in such a way, that it does not bias the measurement and that one can determine precisely the process it originates from. In particular it must pass the trigger criteria and match the trigger object (c.f. Section 5.2).

MC Simulation

Table 6.1: MC samples used for the $b\bar{b}$ and $c\bar{c}$ process simulation.

Process	Generator(s)	Cross-section	UE tune calculation	PDF set
$b\bar{b}$	Pythia 8 B	NLO	A14	NNPDF23LO
$c\bar{c}$	Pythia 8 B	NLO	A14	NNPDF23LO

In contrast to the important $t\bar{t}$ production, MC production of $b\bar{b}$ and $c\bar{c}$ processes have relatively low priority at the LHC. In the ATLAS collaboration no MC samples with exclusive b or c-quarks production existed. Multi-jet samples, that include also the production of light quarks were the only opportunity. The available MC statistics corresponds to an effective luminosity in the order of a view nb^{-1}. Recently, inclusive $b\bar{b}$ and $c\bar{c}$ samples have been produced with a filter that requires at least one muon with $p_{\text{T}} > 15$ GeV. In total 5 million events corresponding to an effective luminosity of 26.1 pb^{-1} was produced. MC statistics, therefore, is the largest contribution to the uncertainty in the scale factor determination.

Table 6.2: Muon triggers suitable for the muon tag selection (see text).

Trigger	Offline p_{T} threshold	Data 2015	Data 2016	Used for
single non-isolated μ	21 GeV	$F_{\mathrm{PS}} = 10$	irregular	2015
single non-isolated μ	25 GeV	$F_{\mathrm{PS}} = 32$	$F_{\mathrm{PS}} = 50$	2016
single non-isolated μ	41 GeV	unprescaled	irregular	2015
single non-isolated μ	51 GeV	unprescaled		2016

The MC samples were produced with a pile-up contribution as expected for the 2016 data taking. For the data taken in 2015 with different pile-up distribution, the MC sample has to be reweighted. In order not to loose statistics due to down-weighting of over-represented events, the relatively small data set taken in 2015 was neglected completely for this measurement.

Trigger Choice and Prescaling Corrections

The triggers selection is justified as follows. Because of the closeness to a jet, the tag muons are usually not triggered due to the isolation requirements in the trigger. Di-lepton triggers (c.f. Section 5.2) have p_{T} thresholds for both leptons and would bias the low-energy probes. Only single muon triggers with low p_{T} thresholds can be used because, as discussed in Section 6.3, HF leptons have rather low p_{T}. The tag and probe transverse momenta are correlated. Thus it is important to include low-energy tag muons.

A list of potentially useful triggers is shown in Table 6.2. Except for the trigger with the highest threshold, all trigger for 2016 are prescaled (see Section 3.2.5).

Prescaling is not taken into account in the MC production, as it would waste computing power. The contribution of events containing a tag muon matching with a prescaled trigger object would, therefore, be overestimated by the prescale factor, F_{PS}. Events with tag muons, matching a combination of triggers with different prescaling, would be overestimated, by a factor which is more difficult to determine.

For this reason, the selection is split into different regions of muon p_{T}. In each region, only one trigger is considered for trigger matching. Although very useful at the beginning of the data taking, two of the triggers were turned off in irregular intervals for several data taking runs in 2016. This necessitates the reduction of the trigger candidates to two remaining triggers with

- muon $p_{\mathrm{T}} \geqslant 51$ GeV and with
- muon p_{T} in the range 25 GeV $\leqslant p_{\mathrm{T}} \leqslant$ 51 GeV.

The tag muon p_{T} distributions without corrections for prescaling are shown in Figure 6.9. Monte Carlo overestimates the data by far for $p_{\mathrm{T}} \leqslant 51$ GeV. A step in the data p_{T} distribution occurs at this transition point between the two triggers.

This makes it necessary to correct for the prescaling in data or MC (so-called unprescaling).

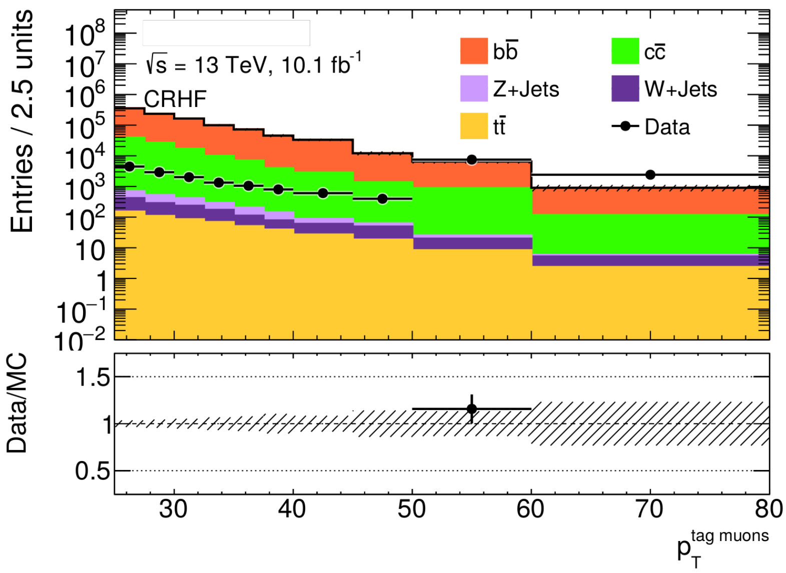

Figure 6.9: p_{T} distributions of tag muons for data and Monte Carlo simulated background processes without corrections for prescaling.

Either the Monte Carlo events have to be scaled down by an average prescale factor or the data event have to be scaled up by the actual prescale factors applied during data taking. Both approaches have been studied and the results differ slightly. Since the number of events with a tag muon with $p_{\mathrm{T}} \geqslant 51$ GeV is only on the order of 10 in the MC samples, rescaling the MC events would induce more uncertainties than re-weighting the data. In Figure 6.9, the luminosity corresponding to the data in the region above 51 GeV is 10.1 fb^{-1}, whereas it is only about 200 pb^{-1} for the region below $p_{\mathrm{T}} = 51$. For other variables the effective luminosity is somewhere between these two values. Weighting the data removes the prescaling effect and restores a continuous p_{T} spectrum of the tag muons.

Therefore, rescaling of the data by the prescale factor associated to each event has been adopted as the best method.

Event Selection

The tag-and-probe events are selected in a control region named CR_{HF} by using the following requirements:

- Exactly one baseline electron or muon (the probe lepton).
- Exactly one b-jet[2].
- Exactly one tag muon satisfying the following requirements:
  - Preselected muon *failing* the overlap removal requirements,
  - close to the b-jet with $\Delta R(\mu, b\text{-jet}) < 0.4$,
  - with $p_T > 25$ GeV and
  - matched to a trigger muon.
- $M_T < 40$ GeV, where M_T is described below.
- $E_T^{miss} < 60$ GeV.

The cuts in this selection are justified as follows. The main backgrounds to the tag-and-probe event selection are $W + jets$ and $t\bar{t}$, both potentially containing tagged b-jets and W bosons. Therefore, prompt leptons from W decays instead of HF leptons are probed in these events. To reduce the contamination by W decays, a cut on the transverse mass M_T

$$M_T = \sqrt{2E_T^{miss} p_T^{probe} \left[1 - \cos(\varphi(E_T^{miss}, p_T^{probe}))\right]} \tag{6.8}$$

of the probe lepton is applied which is the transverse component of the invariant mass of probe lepton and the missing momentum 4-vector, which corresponds to the neutrino in leptonic W decays. The lepton M_T distribution from W occurs has the shape of Jacobian distribution with an edge at the value of the W mass. To further suppress background contributions an E_T^{miss} cut is applied.

Figure 6.10 shows the purity of the Monte Carlo control region CR_{HF} depending on the cuts in E_T^{miss} and M_T.

The cut in M_T turns out to be important to increase the purity on the probe lepton sample especially in the region $p_T \gtrsim 20$ GeV as can be seen in Figure 6.11.

The multiplicity of b-jets is limited to 1, assuming that the second b-jet is not identified in the vicinity of the probe lepton. The selected probe muon would likely not be originated from the second b in $b\bar{b}$ events.

Event Yields

Comparing data and MC yields in CR_{HF} in Figure 6.12 one observes an overall excess of MC events by a factor of 2 while the shapes of the data and MC distribu-

[2] b-tag working point has a 85% efficiency

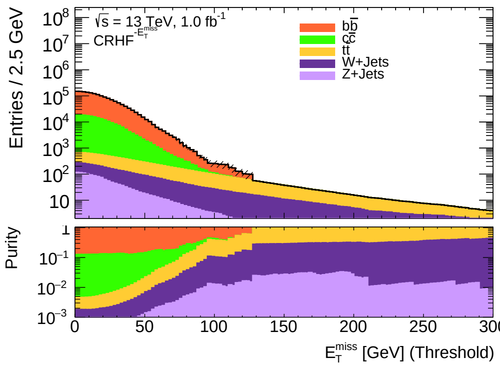

(a) $E_{\mathrm{T}}^{\mathrm{miss}}$ requirement removed

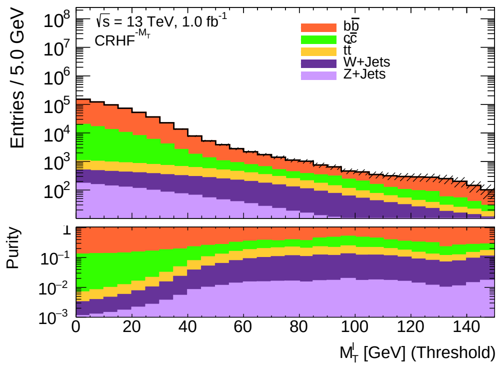

(b) M_{T} requirement removed

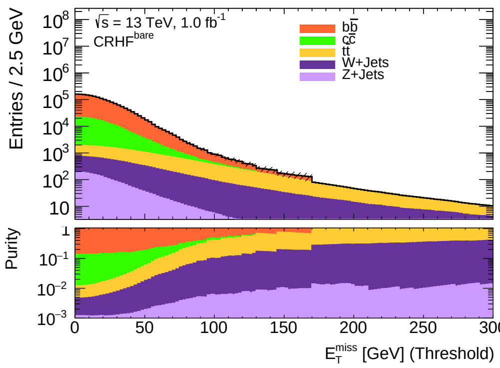

(c) Both requirements removed

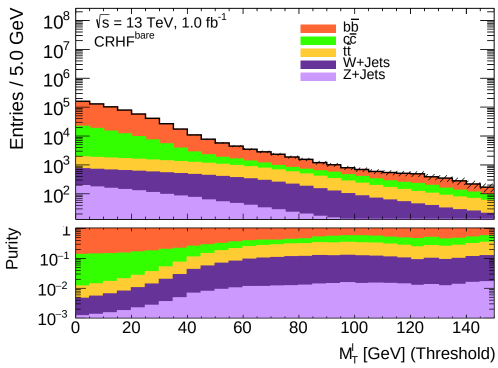

(d) Both requirements removed

Figure 6.10: Event yields, in the control region $\mathrm{CR}_{\mathrm{HF}}$ as a function of the cuts in $E_{\mathrm{T}}^{\mathrm{miss}}$ and M_{T}. The cut in $E_{\mathrm{T}}^{\mathrm{miss}}$ and m_{eff} are omitted in (a,c,d) and in (b,c,d), respectivey.

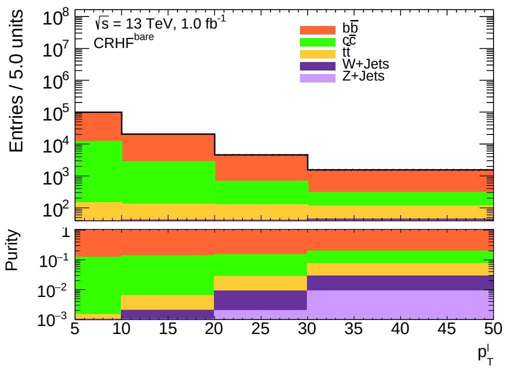

(a)

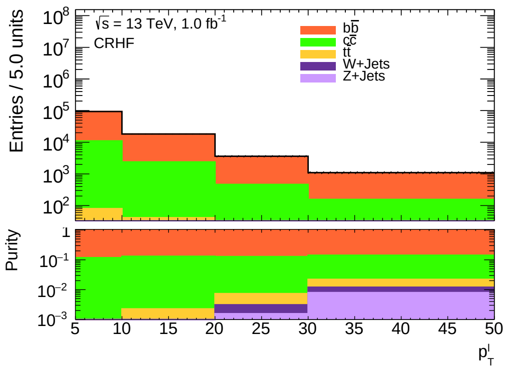

(b)

Figure 6.11: p_{T}-distribution of probe leptons (a) with and (b) without the purification cuts in $E_{\mathrm{T}}^{\mathrm{miss}}$ and M_{T} applied.

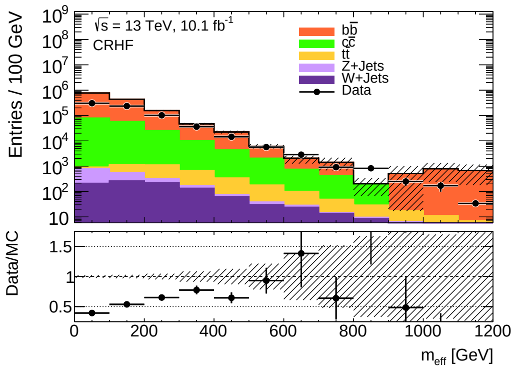

(a) m_{eff}

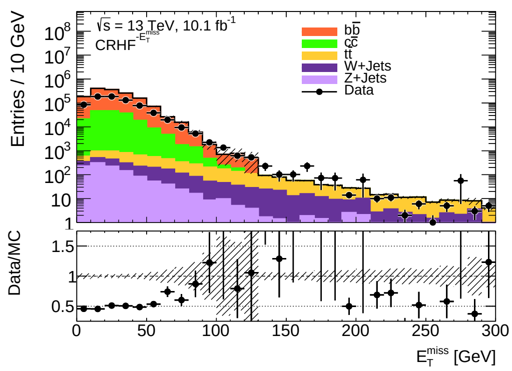

(b) $E_{\text{T}}^{\text{miss}}$

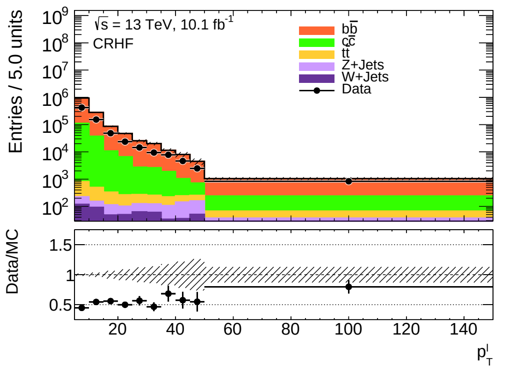

(c) probe lepton p_{T}

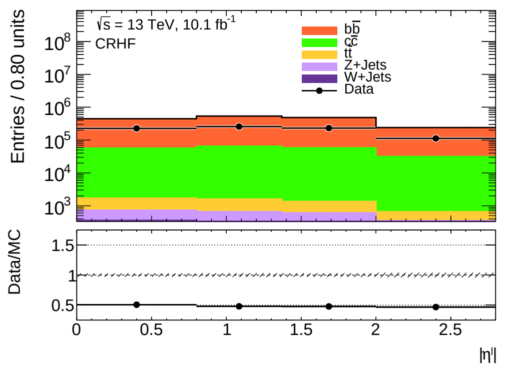

(d) probe lepton $|\eta|$

Figure 6.12: Data and MC yields in CR_{HF} as a function of discriminating variables. In (b) the cut in $E_{\text{T}}^{\text{miss}}$ is removed.

tions agree quite overall. This excess appeared with the updating of the $b\bar{b}$ and $c\bar{c}$ MC samples. Therefore it is suspected, that the new $b\bar{b}$ and $c\bar{c}$ MC simulation does not correctly describe the data. The exact reason for this still has to be identified.

If this assumption is correct, the disagreement will not harm the fake factor measurement because the FFs are measured independently for each sample, where signal and loose lepton identification, are affected by the same overestimation by a factor of 2. Since the fake factor is the ratio of signal and loose lepton yields, the overall normalization cancels.

6.4.2 Scale Factor Results

Fake factors are measured as described in Section 6.3, for both data and MC, as a function of several variables.

The fake factor distributions for data and MC are then devided by each other according to (6.7) to determine the scale factor depending on the variables. Sys-

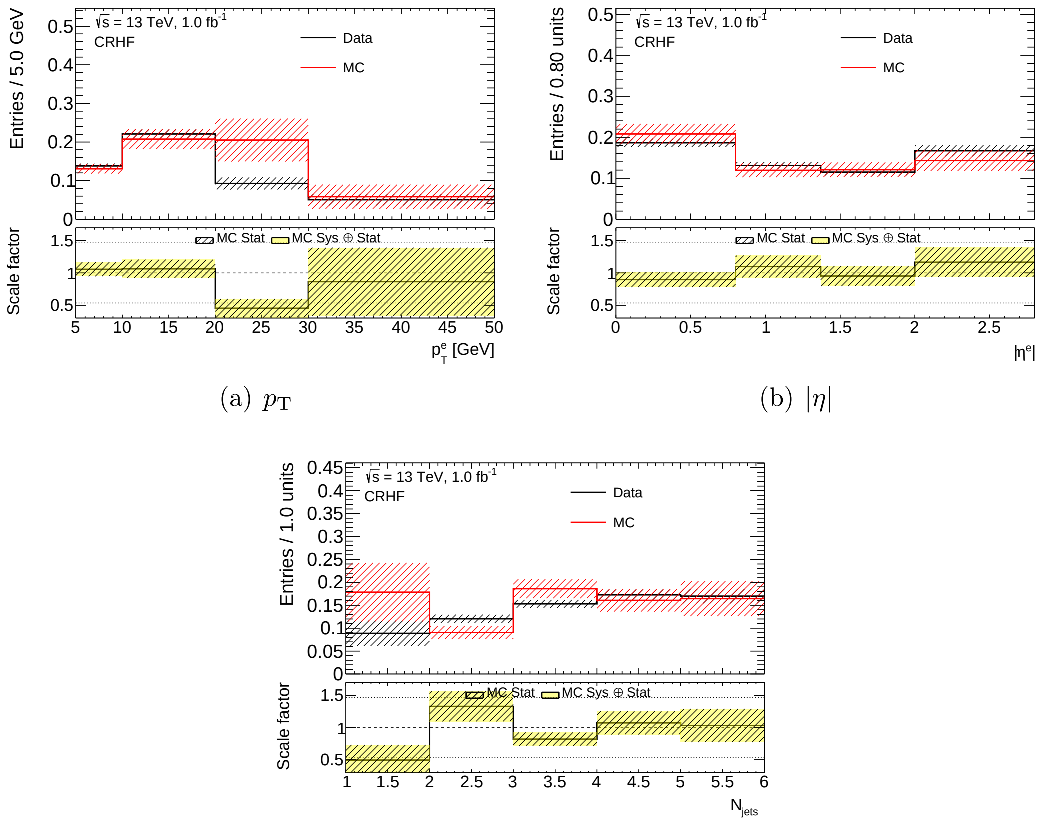

(a) p_{T}

(b) $|\eta|$

(c) jet multiplicity

Figure 6.13: Upper panel: p_{T}, η and jet multiplicity distributions of heavy flavor fake factors for electrons in data (black) and Monte Carlo (red). The ratio in the lower panel corresponds to the scale factor, which shows no significant dependency in the tested variables.

tematic uncertainties are determined by varying the cuts on $E_{\mathrm{T}}^{\mathrm{miss}}$ and M_{T} by ± 10 GeV.

Figure 6.13 shows the p_{T}- and the η-dependence of the electron fake factor in data and MC measured in the HF control data sample $\mathrm{CR}_{\mathrm{HF}}$. The distributions agree within statistical uncertainties (dashed regions in Figure 6.13). The average electron scale factor is found to be

$$sf_{(e)}^{HF} = 1.011 \pm 0.079^{+0.017}_{-0.022},$$

which is much closer to 1 compared to the run 1 value of 0.69 ± 0.05.

In Figure 6.14 the same distributions are shown for muons. Unlike for electrons there is a slight discrepancy between data and MC increasing with $|\eta|$ which is attributed to the type of muon reconstruction as described in Section 4.2 which varies with $\|eta|$. This effect has to be investigated in future. The average muon scale factor is

$$sf_{(\mu)}^{HF} = 0.848 \pm 0.053^{+0.003}_{-0.013},$$

which is very close to the value 0.84 ± 0.11 obtained in run 1. Besides p_{T} and η, other variables were checked for a significant impact on the scale factor, but no further were found influencing it in a relevant magnitude. In total it has been decided to use the global average sf rather than a p_{T}- and η-dependent one.

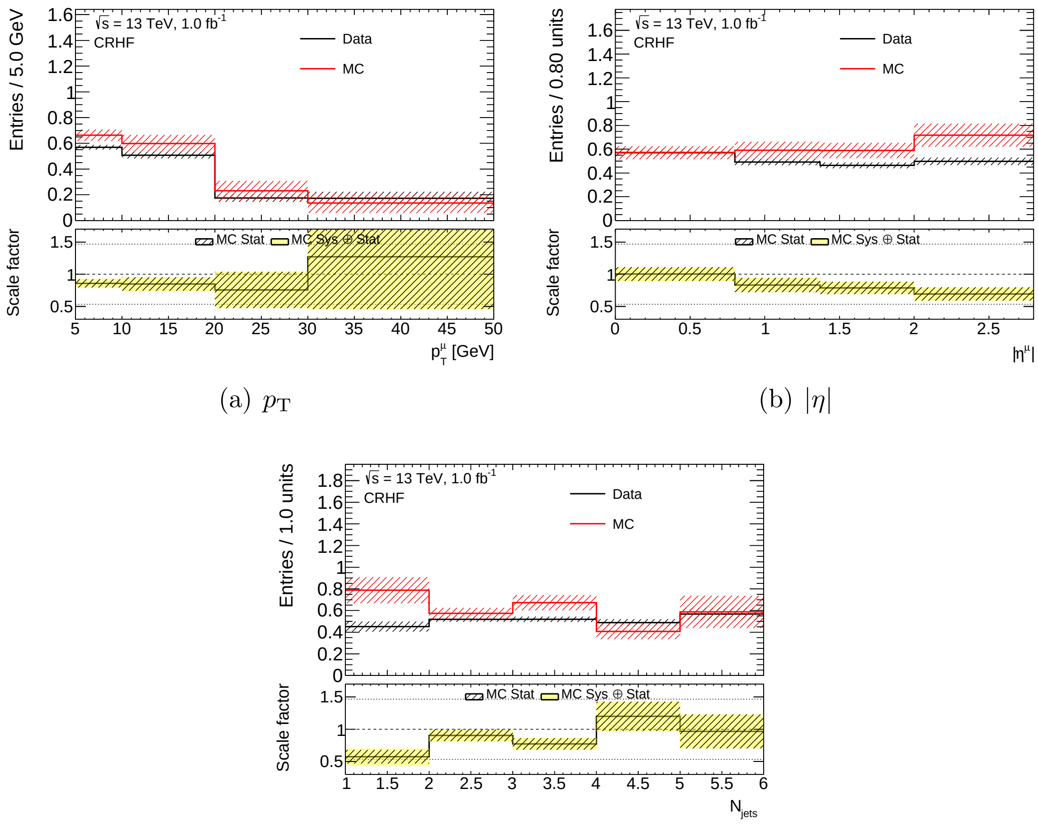

(a) p_{T} (b) $|\eta|$

(c) jet multiplicity

Figure 6.14: Upper panel: p_{T}, η and jet multiplicity distributions of heavy flavor fake factors for muons in data (black) and Monte Carlo (red). The ratio in the lower panel indicates the scale factor. A slight η dependency is visible.

Total Scaled Fake Factor for CR2

Up to now only studies of the the HF scale factors were performed.

The FFs for the soft processes CO and LF also have to be corrected as their modelling may not be correct. This has not been done yet. Therefore, large systematic uncertainties are assigned. A scale factor of 1.00 ± 0.25 is applied, which is on the order of magnitude as measured for HF.

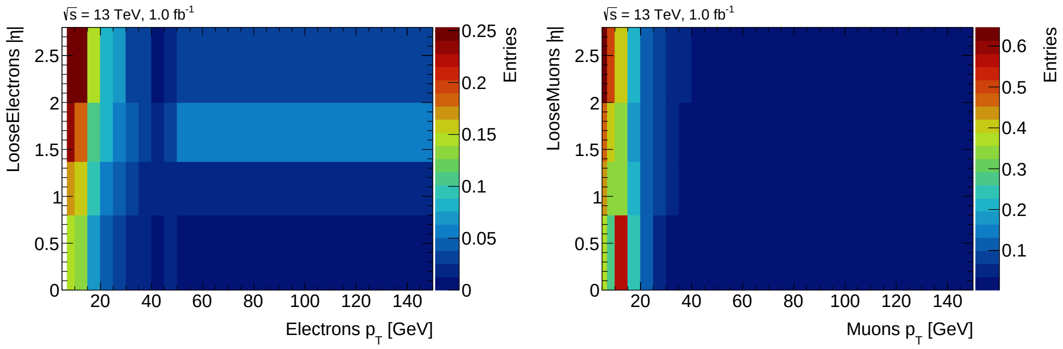

(a) Electrons (b) Muons

Figure 6.15: Fake factor as a function of lepton p_T and $|\eta|$.

The total corrected fake factors are then

$$\begin{aligned} F^{(e)}_{t\bar{t},\mathrm{CO}} &= 0.0327 \pm 0.001(\mathrm{stat}) \pm 0.008(\mathrm{syst}), \\ F^{(\mu)}_{t\bar{t},\mathrm{LF}} &= 0.345 \pm 0.012(\mathrm{stat}) \pm 0.086(\mathrm{syst}), \\ F^{(e)}_{t\bar{t},\mathrm{HF}} &= 0.112 \pm 0.001(\mathrm{stat}) \pm 0.008(\mathrm{syst}), \\ F^{(\mu)}_{t\bar{t},\mathrm{HF}} &= 0.198 \pm 0.001(\mathrm{stat}) \pm 0.012(\mathrm{syst}), \end{aligned}$$

where the statistical uncertainties arise from the statistics of the $t\bar{t}$ MC sample and systematic error represent the total uncertainties in sf. Using the process fractions from Section 6.2 and Equation (6.4), these process dependent fake factors are combined the weighted average fake factors,

$$\begin{aligned} F^{(e)}_{\mathrm{CR2}} &= 0.108 \pm 0.001(\mathrm{stat}) \pm 0.008(\mathrm{syst}), \\ F^{(\mu)}_{\mathrm{CR2}} &= 0.205 \pm 0.001(\mathrm{stat}) \pm 0.016(\mathrm{syst}). \end{aligned}$$

In practice, this global value is not used and only serves for demonstration of the importance of the systematic uncertainties in the HF scale factor. One can see, that the large uncertainties of the other scale factors have a minor impact on the overall uncertainty. In practice the fake factors are applied as a function of the lepton p_T and $|\eta|$ of the loose leptons, in the form of 2D histograms as shown in Figure 6.15.

6.5 Alternative Fake Factor Measurement

An alternative method to determine the fake factor from data is to measure it directly for the relevant process, top-quark pair production. This tag-and-probe approach is inspired by the fake factor studies for the SUSY search in the strong-production channel resulting in either three-lepton or two same-sign leptons [50]. In this chapter preliminary results are presented for comparison to the fake factors derived in the previous sections highlighting advantages and disadvantages of measuring the data's fake factor directly in the $t\bar{t}$ process.

6.5.1 Event Selection

To select $t\bar{t}$ production processes 2 leptons are required. One, referred to as tag, is required to be a rather highly energetic, isolated muon with $p_{\mathrm{T}} > 40$ GeV in order to distinguish it from HF leptons. Due to its isolated nature and the relative high p_{T}, it can be matched to a variety of unprescaled lepton available triggers. Because the triggers are not prescaled, also combinations of them can be used. Studies of an optimum choice of the trigger criteria have not been performed yet, since the $b\bar{b}$-method explained in Section 6.4 had priority. The selection of tag electrons turned out to be problematic and does not increase the statistics as much as expected. Therefore, only muons are used as tag in this approach.

The second lepton, referred to as probe, must have the same sign of the electric charge as the tag muon, with the purpose to reject prompt leptons originating from second top-quark decay. Two prompt leptons should not share the same sign, as both come from the decays of two oppositely charged bottom-quarks.

To assure $t\bar{t}$ production, at least one b-jet is demanded. As in Section 6.4, the second b-jet is likely to be rejected by the overlap removal with the probe lepton. Therefore a second b-jet might indicate, that the probe lepton does not origin from a b-jet. Furthermore, since the second top quark is supposed to decay hadronically, it results in further jets. Thus the total number of jets is at least three. In addition, a minimum $E_{\mathrm{T}}^{\mathrm{miss}}$ is required to suppress contributions from the diboson production processes, $ZZ \to \ell^+\ell^- q\bar{q}$ and $WZ \to \ell^+\ell^- qq'$, and the $b\bar{b}$ production.

The remaining background after this selection is dominated by $W+jets$ production. Using the truth information (c.f. Section 4.1) it turns out, that the probing of muons from $W+jets$ events actually are from heavy flavor decays (HF muons). To further reduce this background, for probing electrons, one can still require higher jet (b-jet) multiplicities at the cost of loosing statistics (c.f Figure 6.16).

Another source of background is due to so-called charge-flip. A sizeable contribution to the selected event sample arises from misreconstructed lepton charges in $t\bar{t}$ events. This happens predominantly for electrons: When an electron passes detector material (e.g. in the inner detector), it can produce hard Bremsstrahlung photons which can convert into e^+e^- pairs. If the conversion electron with largest

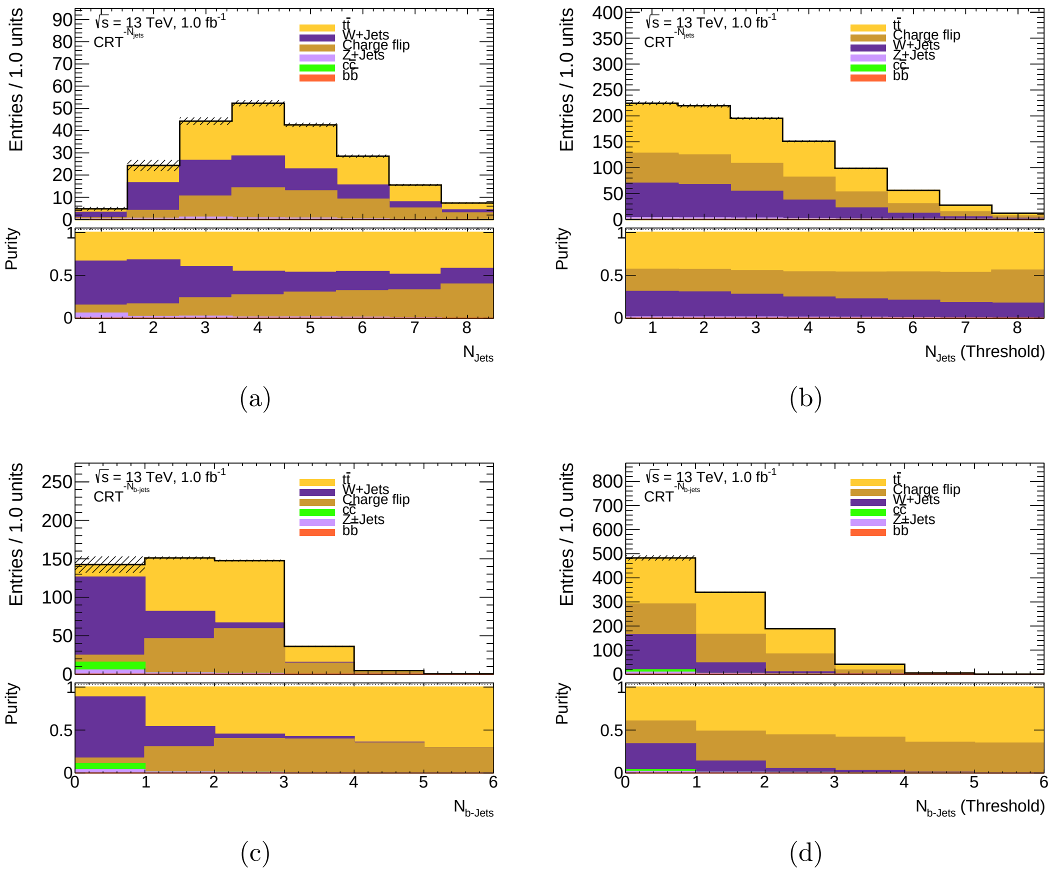

Figure 6.16: Event yields and purity of the $t\bar{t}$ control region selection $\mathrm{CR_T}$ as a function of jet (a) and b-jet (c) multiplicity and the cuts in these variables (b,d).

p_T has opposite charge compared to the original prompt lepton, the wrong sign can be assigned to the electron track leading to a charge-flip event. This results in undesired non-HF probe electrons contributing about half of the total $t\bar{t}$ event yields for probe electron yields.

The complete $\mathrm{CR_T}$ selection is:

- Exactly one tag muon with
  - $p_\mathrm{T} > 40$ GeV,
  - Passing signal requirements and
  - Matches to trigger muon.
- At least one b-tagged signal jet.
- At least two further signal jets.
- Exactly one probe lepton with same sign as tag.
- $E_\mathrm{T}^\mathrm{miss} > 90$ GeV

Figure 6.17 shows the comparison between the event yields in data and MC simulation after the selection.

For a fully data-driven method, the contribution of charge-flip is estimated by using reweighted data events in a further control region. This region is defined by the same selection as $\mathrm{CR_T}$ but with the charge sign requirement inverted. The contribution of charge-flip in $\mathrm{CR_T}$ can be estimated by applying the rate of a charge-flip probability to the opposite sign control region. This charge-flip rate has not been determined yet from data. In the meantime, it is estimated from Monte Carlo simulation.

Since the charge-flip only occurs for electrons, the muon FF determination is already fully data-driven.

6.5.2 Results

Despite the open issues mentioned, the fake factors can be calculated, however with relatively large systematic uncertainties for electrons. The average FFs for electrons and muons determined directly from $t\bar{t}$ data are:

$$F^{(e)}_{\mathrm{CR_T}} = 0.109 \pm 0.016, \qquad F^{(e)}_{\mathrm{CR_{HF}}} = 0.112 \pm 0.009,$$
$$F^{(\mu)}_{\mathrm{CR_T}} = 0.329 \pm 0.034, \qquad F^{(\mu)}_{\mathrm{CR_{HF}}} = 0.198 \pm 0.013.$$

Compared to the HF sf determined weighted average FFs from Sections 6.3 and 6.4. Figure 6.18 shows their p_{T} dependence.

Following the procedure in Section 6.4, scale factors:

$$sf^{HF}_{(e)} = 0.728 \pm 0.108, \qquad sf^{HF}_{(\mu)} = 0.909 \pm 0.103,$$

can be derived and compared to the scale factors for $\mathrm{CR_{HF}}$ from Section 6.4:

$$sf^{HF}_{(e)} = 1.011 \pm 0.079^{+0.017}_{-0.022},$$
$$sf^{HF}_{(\mu)} = 0.848 \pm 0.053^{+0.003}_{-0.013}.$$

Both agree within the relatively large uncertainties.

Figure 6.19 shows the p_{T}- and $|\eta|$-dependence of the scale factors obtained in $\mathrm{CR_T}$.

6.5.3 Discussion

The advantages of the $t\bar{t}$-method is of course the direct measurement of the HF fake factor in the relevant background process. Corrections for possible sf dependence on the hard process are not necessary.

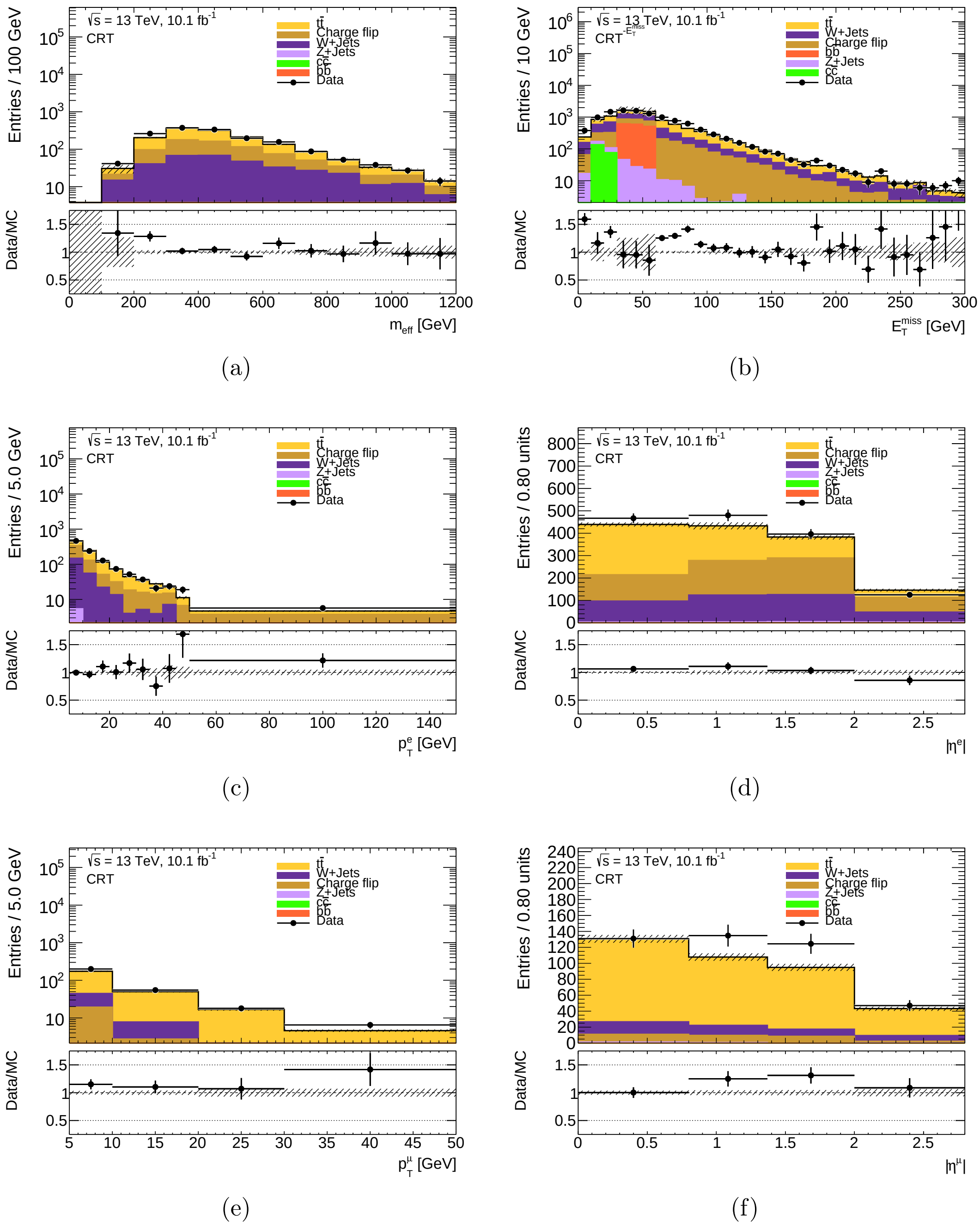

Figure 6.17: Comparison of data and MC yields in the control region $\mathrm{CR_T}$ as function of discriminating variables. In (b) the $E_{\mathrm{T}}^{\mathrm{miss}}$-cut is removed.

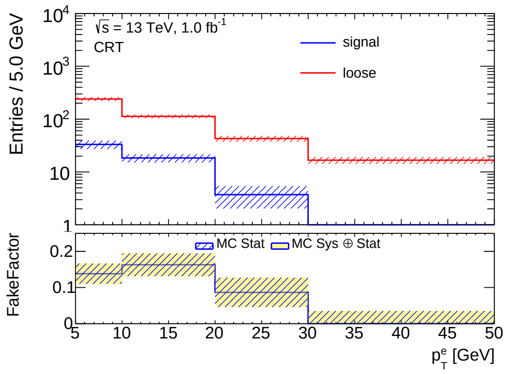

(a) Electron FF from $t\bar{t}$ data in $\mathrm{CR_T}$, p_T

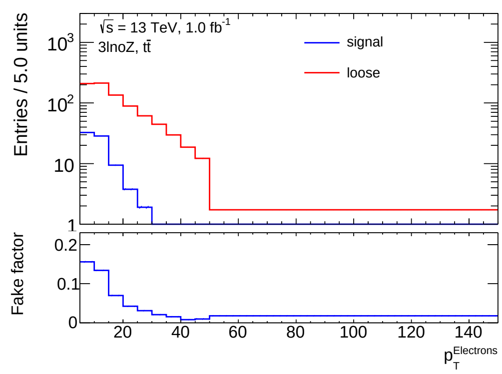

(b) Electron FF from $t\bar{t}$ data in MC × sf, p_T

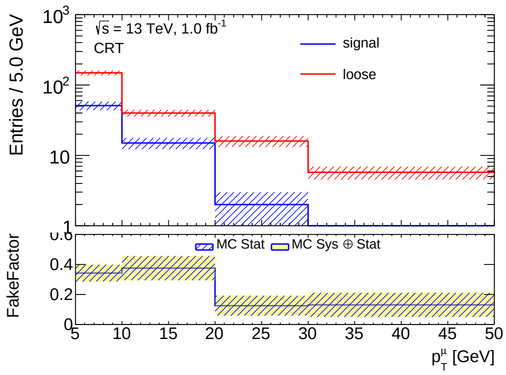

(c) Muon FF in $\mathrm{CR_T}$, p_T

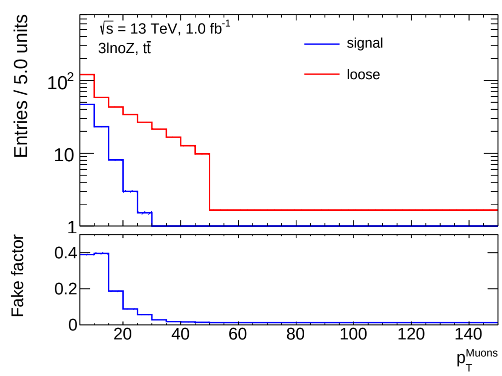

(d) Muon FF in MC × sf, p_T

Figure 6.18: Comparison of the $t\bar{t}$ and the HF MC$\times sf(\mathrm{CR_{HF}})$, fake factors as a functin of the probe leptons p_T resulting from two different methods.

Scale factors obtained by comparing data and MC for $b\bar{b}$ production take into account possible mismodelings of these events which depends on the MC generators. In fact, different generators are used to simulate $t\bar{t}$ events (used for computation of MC FF in Section 6.3) and $b\bar{b}$ production (used for the HF scale factor in Section 6.4). This doubt does not arise for a scale factor measured in the $t\bar{t}$ data sample. Also, the available $t\bar{t}$ MC samples are much larger and have been validated by several analysis groups. Mismodelings is therefore less likely than for the $b\bar{b}$ sample has in $\mathrm{CR_{HF}}$.

There are, however, disadvantages, which lead to the decision to use the data control region $\mathrm{CR_{HF}}$ for the measurement of the scale factors. $\mathrm{CR_{HF}}$ is much purer in HF leptons than $\mathrm{CR_T}$. For the calculation of the electron FF the charge-flip rate has to be determined in a separate measurement. Furthermore, the number of events in $\mathrm{CR_T}$ corresponding to 10 fb^{-1} of data is on the order of $\mathcal{O}(10^3)$, which is much less than in $\mathrm{CR_{HF}}$ which contains $\mathcal{O}(10^6)/F_\mathrm{prescale}$ events. In addition, the probe lepton p_T is limited to below ≈ 50 GeV even in data.

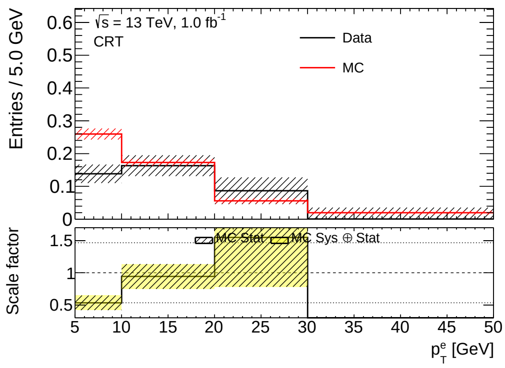

(a) Electron sf, p_{T}

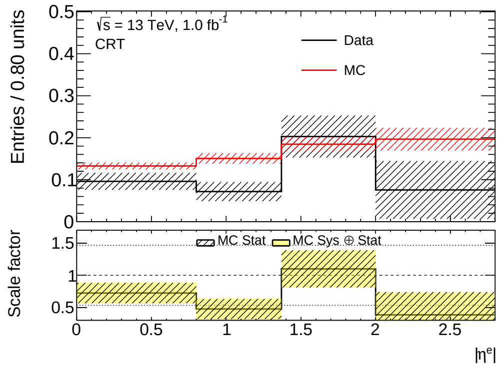

(b) Electron sf, $|\eta|$

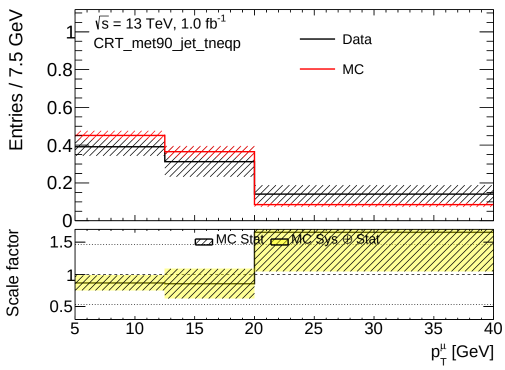

(c) Muon sf, p_{T}

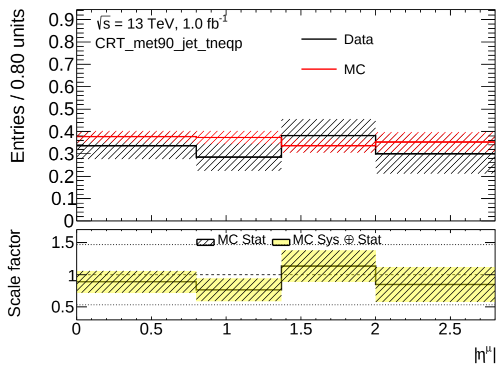

(d) Muon sf, $|\eta|$

Figure 6.19: p_{T}- and $|\eta|$-dependence of the scale factors determined in $\mathrm{CR_T}$ for probe leptons (see text).

Chapter 7

Results

The SUSY search in events with at least four leptons is constrained by the existence of a certain kind of background, the so-called 2-fake lepton reducible background. It is characterized by two objects contributing to the lepton multiplicity but not being real leptons emerging in the primary process. This thesis focuses on the estimation of this type of background.

A data-driven method was developed to estimate that background from a measurement in a dedicated control regions. That method exploits the differences in object characteristics between prompt and fake leptons on a statistical basis. Fake leptons are rejected in the majority of cases due to isolation and impact parameter requirements with a statistical determinable rate. These control regions require not four but only two signal leptons and 2 additional leptons with looser quality requirements.

The contributions of different mechanisms leading to reducible background are investigated. It was found, that the leptonic decay of heavy flavor hadrons in top-quark pair production events is the most dominant source of fake background.

Fake factors, which is the extrapolation factor from control to signal regions, have been determined in a $t\bar{t}$ MC sample considering all relevant mechanisms producing reducible background. The global average of the fake factor, responsible for the leptonic heavy flavor hadron decay, for electrons and muons is

$$F^{(e)}_{t\bar{t},\mathrm{HF}} = 0.107 \pm 0.001$$
$$F^{(\mu)}_{t\bar{t},\mathrm{HF}} = 0.234 \pm 0.001.$$

The fake factor for the sub-dominant conversion electrons is found to be

$$F^{(e)}_{t\bar{t},\mathrm{CO}} = 0.0327 \pm 0.001,$$

and fake leptons from light flavor hadrons have an averaged fake factor of

$$F^{(\mu)}_{t\bar{t},\mathrm{LF}} = 0.345 \pm 0.012.$$

The uncertainties are statistical and arise from the number of generated $t\bar{t}$ events.

To account for potential differences in data and simulation a scale factor was measured for the heavy flavor fake factors. It has been measured in two different approaches. The first used a $b\bar{b}$ enriched selection, which tagged one of the b-quarks by selecting a non-isolated muon within a b-tagged jet and probed a second solitary baseline muon in that event. Its small contamination of real leptons from primary $t\bar{t}$ and $W+jets$ processes was rejected using an upper M_T and a $E_{\mathrm{T}}^{\mathrm{miss}}$ cut (utilized as W-boson veto). Comparison of data measurements with simulations gives scale factors for electrons and muons of

$$sf_{(e)}^{HF} = 1.011 \pm 0.098$$
$$sf_{(\mu)}^{HF} = 0.848 \pm 0.061.$$

A second approach was presented that was doubted to be useful for a while, since it yields less statistics. It measures the scale factor in a $t\bar{t}$ enriched region. Tagging a high energetic muon from the top decay and requiring one b-jet in the event, a lepton of the same sign as the tag is supposed to be originated from a leptonic b-hadron decay, thus a heavy flavor fake. It turns out that the effect of misidentified electron charges induce a high contamination from non-heavy-flavor electrons, directly produced in the $t\bar{t}$ process. It requires further investigations, but this approach already delivered a resilient muon scale factor,

$$sf_{(\mu)}^{HF} = 0.909 \pm 0.103,$$

withing statistical agreement with the one measured in the $b\bar{b}$ enriched region.

This modeling of the reducible 2-fake background, combined with the simulation based estimation of irreducible background and 1-fake background, is tested in a low-m_{eff} validation region, defined to be disjoint to the signal regions. Its background model is the same as in the signal regions, with irreducible background and 1-fake background modelled by MC simulation.

Contributions obtained by the fake factor method were found to be 16 ± 6 events in in 13.3 fb^{-1} in this validation region. Its uncertainty is predominantly statistical and determined by the yields in the control regions. The total background from Standard Model in the validation region is 51 ± 6, which is in good agreement to the measured 53 events.. Observed and expected yields with respect to m_{eff} in the VR can be seen in the lower m_{eff} bins in Figure 7.1(a).

Expected 2-fake reducible background in the SRA (SRB) is found to be 0.48 ± 0.24 (0.11 ± 0.05) events in 13.3 fb^{-1}.

Together with the simulation based expectation, this adds up to 3.6 ± 0.6 in SRA, while no events are observed in SRB. The observations are consistent with the Standard Model expectation. The m_{eff} and $E_{\mathrm{T}}^{\mathrm{miss}}$ distributions for all events passing the Z veto are shown in Figure 7.1.

For the statistical interpretation, The HistFitter [51] software framework is used. To set the exclusion limits in the $LL\bar{E}12k$ models, where the lightest supersymmetric particle may decay to light leptons, the signal region with the best expected exclusion limit is used. For the exclusion limits, the observed and expected 95% CL limits are calculated using an Asimov dataset for each SUSY

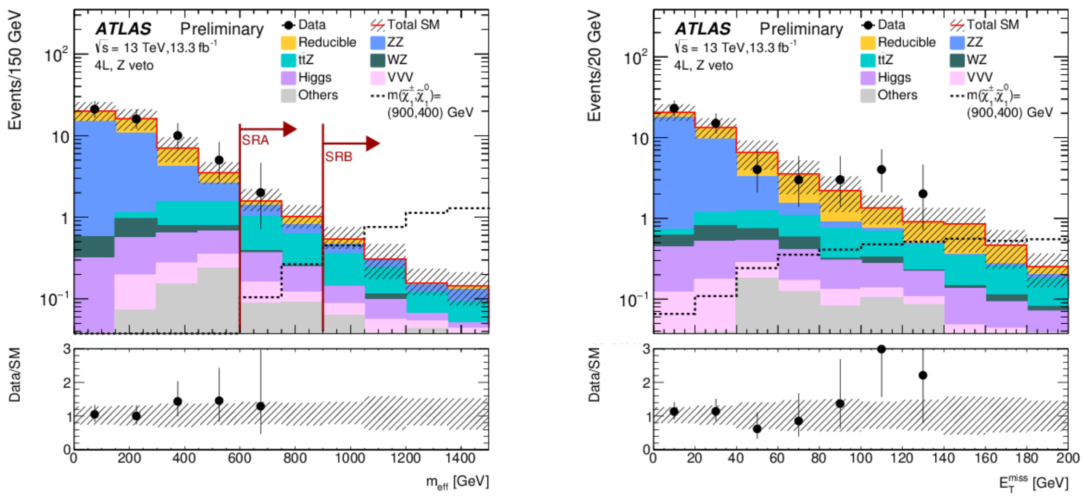

(a) m_{eff} (b) $E_{\text{T}}^{\text{miss}}$

Figure 7.1: Distributions for m_{eff} and $E_{\text{T}}^{\text{miss}}$in data. The estimated SM backgrounds and an example SUSY scenario in four-lepton events that pass the Z veto requirement are shown. The irreducible and 1-fake lepton backgrounds are estimated from MC simulation while the 2-fake lepton background is estimated from data. Statistical and systematic uncertainties are indicated by the shaded band. The red arrows highlight the m_{eff} selections in the signal regions. The region with $m_{\text{eff}} < 600$ GeV is used to validate the SM background modelling [20].

model point, taking into account systematical uncertainties. Figure 7.2 shows the exclusion contour of the $LL\bar{E}12k$ model, where $\tilde{\chi}_0^{\pm}$ with masses up to 1.14 TeV are excluded for $\tilde{\chi}_1^0$-masses above 500 GeV. The sensitivity is reduced where the decay products are collimated and boosted for large mass difference between the $\tilde{\chi}_1^0$ and the $\tilde{\chi}_0^{\pm}$, which itself is excluded for masses up to 1.07 GeV. This extents the limits set in Ref. [16] by around 400 GeV.

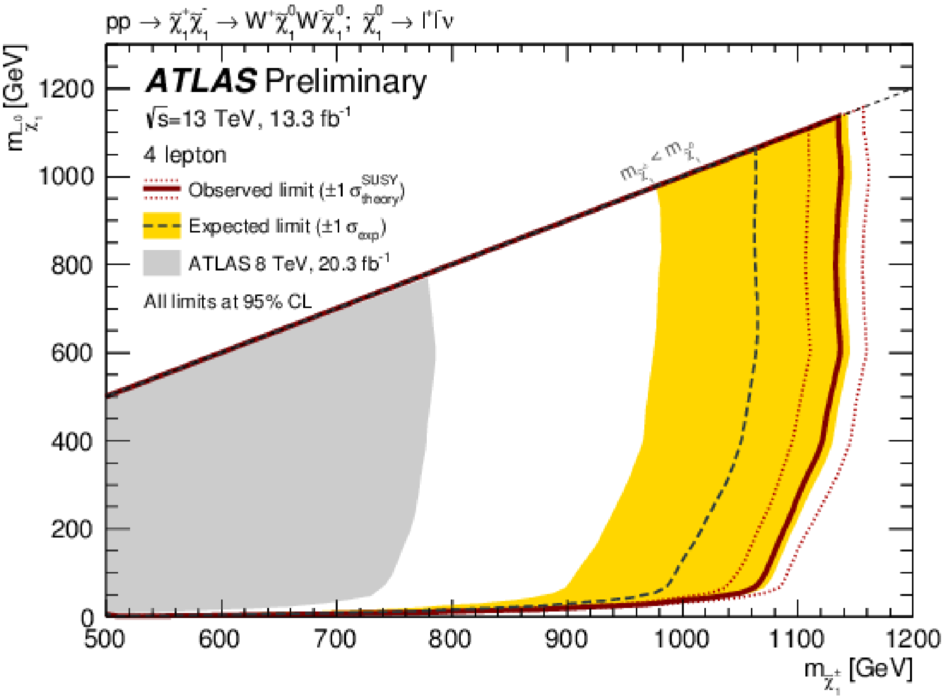

Figure 7.2: The 95% CL exclusion limits on chargino production with indirect RPV decays via λ_{12k}, where $k \in 1, 2$. Reported in [20]. The grey area indicates the limit measured with $\sqrt{s} = 8$ TeV from from Ref. [52].

Chapter 8

Conclusions

A data-driven method, the Fake Faktor (FF) method, has been developed for the estimation of the reducible background of Standard Model processes, dominantly top-quark pair production, with misidentified (fake) leptons contributing to the signal regions in the R-parity violating decays of supersymmetric particles to final states with at least four leptons.

It involves the determination of scale factors (fake factors) between data control regions and the signal regions. The fake factors are determined from Monte Carlo (MC) simulated event samples using truth information. A correction (scale) factor to the fake factor from simulation was determined from data in two independent event selections, one enriched in $b\bar{b}$ and one in $t\bar{t}$ production. Both approaches are resilient. But as new $b\bar{b}$ MC samples are in production, a redetermination of the scale factor in the near future using these new samples may deliver still more accurate results.

Furthermore, the determination of the correction factor for electrons, from the $t\bar{t}$ enriched data region, uses MC information. Further investigations are planned to make also the determination of the electron scale factor fully data-driven.

The results of this analysis are based on 13.3 fb^{-1} of proton-proton collision data recorded by the ATLAS detector at the LHC at a center-of-mass energy of 13 TeV in 2015 and 2016. In a selection of final states with at least four light leptons, which have to pass a Z veto and a effective mass cut, no significant excess derived over the Standard Model background was observed. Exclusion limits for a simplified SUSY model assuming pair production of charginos decaying into neutralinos, with subsequent R-parity violating decays into two light leptons. Chargino masses up to 1.14 TeV have been excluded for large neutralino masses.

This analysis is planned to be extended to include hadronically decaying tau leptons in the signal final state as well as scenarios with neutralinos decaying to lepton pairs via Z-bosons.

Further SUSY models will be considered and their signal will be modeled to improve sensitivity to them.

Investigations for more data-driven background estimations are in progress and develop additional control regions also for the already existent signal regions.

A paper is planned to include all these progressing studies by Moriond.

Bibliography

[1] M. Gell-Mann, *A Schematic Model of Baryons and Mesons*, Phys. Lett. **8** (1964) 214–215.

[2] S. Weinberg, *A Model of Leptons*, Phys. Rev. Lett. **19** (1967) 1264–1266. http://link.aps.org/doi/10.1103/PhysRevLett.19.1264.

[3] S. L. Glashow, *Partial Symmetries of Weak Interactions*, Nucl. Phys. **22** (1961) 579–588.

[4] ATLAS Collaboration, *Observation of a new particle in the search for the Standard Model Higgs boson with the ATLAS detector at the LHC*, Phys. Lett. B **716** (2012) 1 – 29.

[5] C. Collaboration, *Observation of a new boson at a mass of 125 GeV with the CMS experiment at the LHC*, Phys. Lett. B **716** (2012) 30 – 61. http://www.sciencedirect.com/science/article/pii/S0370269312008581.

[6] A. Einstein, *Die Grundlage der allgemeinen Relativitätstheorie*, Annalen der Physik **354** (1916) 769–822.

[7] F. Zwicky, *Republication of: The redshift of extragalactic nebulae*, General Relativity and Gravitation **41** no. 1, (2009) 207–224. http://dx.doi.org/10.1007/s10714-008-0707-4.

[8] V. Trimble, *Existence and Nature of Dark Matter in the Universe*, Annual Review of Astronomy and Astrophysics **25** no. 1, (1987) 425–472, http://dx.doi.org/10.1146/annurev.aa.25.090187.002233. http://dx.doi.org/10.1146/annurev.aa.25.090187.002233.

[9] A. G. Riess, A. V. Filippenko, P. Challis, A. Clocchiatti, A. Diercks, P. M. Garnavich, R. L. Gilliland, C. J. Hogan, S. Jha, R. P. Kirshner, B. Leibundgut, M. M. Phillips, D. Reiss, B. P. Schmidt, R. A. Schommer, R. C. Smith, J. Spyromilio, C. Stubbs, N. B. Suntzeff, and J. Tonry, *Observational Evidence from Supernovae for an Accelerating Universe and a Cosmological Constant*, The Astronomical Journal **116** no. 3, (1998) 1009. http://stacks.iop.org/1538-3881/116/i=3/a=1009.

[10] P. J. E. Peebles and B. Ratra, *The cosmological constant and dark energy*, Rev. Mod. Phys. **75** (2003) 559–606. http://link.aps.org/doi/10.1103/RevModPhys.75.559.

[11] A. D. Sakharov, *Violation of CP invariance, C asymmetry, and baryon asymmetry of the universe*, Soviet Physics Uspekhi **34** no. 5, (1991) 392.

http://stacks.iop.org/0038-5670/34/i=5/a=A08.

[12] S. P. Martin, *A Supersymmetry primer*, Adv. Ser. Direct. High Energy Phys.18 (1998).

[13] H. Dreiner, *An introduction to explicitR-parity violation*, Pramana **51** no. 1, (1998) 123–133. http://dx.doi.org/10.1007/BF02827485.

[14] T. A. Collaboration, *The ATLAS Experiment at the CERN Large Hadron Collider*, J INSTRUM **3** (2008) S08003. http://stacks.iop.org/1748-0221/3/i=08/a=S08003.

[15] L. Evans and P. Bryant, *LHC Machine*, JINST **3** (2008) S08001.

[16] ATLAS, *Search for supersymmetry in events with four or more leptons in* $\sqrt{s} = 8$ TeV *pp collisions with the ATLAS detector*, Phys. Rev. D **90** (2014) 052001.

[17] M. Ratz, "Notizen vorlesung quantenfeldtheorie." Technische Universität München.

[18] S. Dimopoulos and H. Georgi, *Softly Broken Supersymmetry and SU(5)*, Nucl. Phys. **B193** (1981) 150–162.

[19] R. Barbier, C. Bérat, M. Besançon, M. Chemtob, A. Deandrea, E. Dudas, P. Fayet, S. Lavignac, G. Moreau, E. Perez, and Y. Sirois, *R-Parity-violating supersymmetry*, Physics Reports **420** no. 1–6, (2005) 1 – 195. http://www.sciencedirect.com/science/article/pii/S0370157305003327.

[20] ATLAS, *Search for supersymmetry in events with four or more leptons in* $\sqrt{s} = 13$ *TeV pp collosions using* 13.3 fb^{-1} *of ATLAS data*, ATLAS-CONF-SUSY-2016-01 (2016).

[21] ATLAS Collaboration, "Constraints on promptly decaying supersymmetric particles with lepton-number- and R-parity-violating interactions using Run-1 ATLAS data." ATLAS-CONF-2015-018, 2015. http://cdsweb.cern.ch/record/2017303.

[22] B. Fuks, M. Klasen, D. R. Lamprea, and M. Rothering, *Gaugino production in proton-proton collisions at a center-of-mass energy of 8 TeV*, JHEP **10** (2012) 081, arXiv:1207.2159 [hep-ph].

[23] B. Fuks, M. Klasen, D. R. Lamprea, and M. Rothering, *Precision predictions for electroweak superpartner production at hadron colliders with Resummino*, Eur. Phys. J. C **73** (2013) 2480, arXiv:1304.0790 [hep-ph].

[24] O. S. Brüning, P. Collier, P. Lebrun, S. Myers, R. Ostojic, J. Poole, and P. Proudlock, *LHC Design Report.* CERN, Geneva, 2004. https://cds.cern.ch/record/782076.

[25] ATLAS Collaboration, G. Aad et al., *Performance of the ATLAS Trigger System in 2010*, Eur. Phys. J. **C72** (2012) 1849, arXiv:1110.1530 [hep-ex].

[26] A. Collaboration, *2015 start-up trigger menu and initial performance assessment of the ATLAS trigger using Run-2 data*, ATL-DAQ-PUB-2016-001 no. ATL-DAQ-PUB-2016-001, (2016). `https://cds.cern.ch/record/2136007`.

[27] T. Sjostrand, S. Mrenna, and P. Z. Skands, *PYTHIA 6.4 Physics and Manual*, JHEP **05** (2006) 026, `arXiv:hep-ph/0603175 [hep-ph]`.

[28] T. Sjöstrand, S. Mrenna, and P. Skands, *A brief introduction to PYTHIA 8.1*, Comput. Phys. Commun. **178** (2008) 852 – 867. `http://www.sciencedirect.com/science/article/pii/S0010465508000441`.

[29] T. Sjöstrand, S. Ask, J. R. Christiansen, R. Corke, N. Desai, P. Ilten, S. Mrenna, S. Prestel, C. O. Rasmussen, and P. Z. Skands, *An Introduction to PYTHIA 8.2*, Comput. Phys. Commun. **191** (2015) 159–177, `arXiv:1410.3012 [hep-ph]`.

[30] T. Gleisberg, S. Hoeche, F. Krauss, M. Schonherr, S. Schumann, F. Siegert, and J. Winter, *Event generation with SHERPA 1.1*, JHEP **02** (2009) 007, `arXiv:0811.4622 [hep-ph]`.

[31] T. Gleisberg, S. Höche, F. Krauss, M. Schönherr, S. Schumann, et al., *Event generation with SHERPA 1.1*, JHEP **02** (2009) 007, `arXiv:0811.4622 [hep-ph]`.

[32] J. Alwall, M. Herquet, F. Maltoni, O. Mattelaer, and T. Stelzer, *MadGraph 5 : Going Beyond*, JHEP **06** (2011) 128, `arXiv:1106.0522 [hep-ph]`.

[33] S. Alioli, P. Nason, C. Oleari, and E. Re, *A general framework for implementing NLO calculations in shower Monte Carlo programs: the POWHEG BOX*, JHEP **06** (2010) 043, `arXiv:1002.2581 [hep-ph]`.

[34] J. Alwall, R. Frederix, S. Frixione, V. Hirschi, F. Maltoni, O. Mattelaer, H. S. Shao, T. Stelzer, P. Torrielli, and M. Zaro, *The automated computation of tree-level and next-to-leading order differential cross sections, and their matching to parton shower simulations*, JHEP **07** (2014) 079, `arXiv:1405.0301 [hep-ph]`.

[35] ATLAS Collaboration, G. Aad et al., *The ATLAS Simulation Infrastructure*, Eur. Phys. J. **C70** (2010) 823–874, `arXiv:1005.4568 [physics.ins-det]`.

[36] GEANT4 Collaboration, S. Agostinelli et al., *GEANT4: A Simulation toolkit*, Nucl. Instrum. Meth. **A506** (2003) 250–303.

[37] ATLAS Collaboration, "Luminosity public results run2." `https://twiki.cern.ch/twiki/bin/view/AtlasPublic/LuminosityPublicResultsRun2`.

[38] ATLAS, *Electron identification measurements in ATLAS using* $\sqrt{s} = 13$ TeV *data with 50 ns bunch spacing*, ATL-PHYS-PUB-2015-041 (2015). `http://cdsweb.cern.ch/record/2048202`.

[39] ATLAS, *Electron efficiency measurements with the ATLAS detector using*

the 2015 LHC proton-proton collision data, ATLAS-CONF-2016-024 (2016).

[40] ATLAS, *Muon reconstruction performance of the ATLAS detector in proton–proton collision data at* $\sqrt{s} = 13$ TeV, Eur. Phys. J. C 76 (2016) 292 (2016).

[41] ATLAS Collaboration, G. Aad et al., *Muon reconstruction performance of the ATLAS detector in proton–proton collision data at* $\sqrt{s}$ *=13 TeV*, Eur. Phys. J. **C76** (2016) 292, `arXiv:1603.05598 [hep-ex]`.

[42] M. Cacciari, G. P. Salam, and G. Soyez, *The Anti-k(t) jet clustering algorithm*, JHEP **04** (2008) 063, `arXiv:0802.1189 [hep-ph]`.

[43] ATLAS Collaboration, "Forward Jet Vertex Tagging: A new technique for the identification and rejection of forward pileup jets." ATL-PHYS-PUB-2015-034, 2015. `http://cdsweb.cern.ch/record/2042098`.

[44] "Particle data group live." `http://pdglive.lbl.gov/`.

[45] *Expected performance of the ATLAS b-tagging algorithms in Run-2*, Tech. Rep. ATL-PHYS-PUB-2015-022, CERN, Geneva, Jul, 2015. `https://cds.cern.ch/record/2037697`.

[46] ATLAS, *Performance of missing transverse momentum reconstruction for the ATLAS detector in the first proton-proton collisions at s =13 TeV*, ATL-PHYS-PUB-2015-027 (2015). `http://cds.cern.ch/record/2037904`.

[47] J. J. Junggeburth, *Search for Supersymmetry with R-parity violation in leptonic final states with the ATLAS detector at 13 TeV center-of-mass energy*, Master's thesis, Munich, Max Planck Inst., 2015-12-21. `http://inspirehep.net/record/1429418/files/fulltext_XfRgkY.pdf`.

[48] S. Frixione and B. R. Webber, *Matching NLO QCD computations and parton shower simulations*, JHEP **06** (2002) 029, `arXiv:hep-ph/0204244`.

[49] T. Sjöstrand, S. Mrenna, and P. Z. Skands, *PYTHIA 6.4 Physics and Manual*, JHEP **0605** (2006) 026, `arXiv:hep-ph/0603175`.

[50] ATLAS, *Supporting note for Search for strongly produced superpartners in final states with same-sign leptons or three leptons and jets in pp collisions at* $\sqrt{s} = 13$ TeV, ATL-COM-PHYS-2015-1150 (2016).

[51] M. Baak, G. J. Besjes, D. Côte, A. Koutsman, J. Lorenz, and D. Short, *HistFitter software framework for statistical data analysis*, Eur. Phys. J. C **75** (2015) 153, `arXiv:1410.1280 [hep-ex]`.

[52] ATLAS Collaboration, *Search for supersymmetry in events with four or more leptons in* $\sqrt{s} = 8$ *TeV pp collisions with the ATLAS detector*, Phys. Rev. D **90** (2014) 052001, `arXiv:1405.5086 [hep-ex]`.

List of Figures

List of Tables